Investigations of quantum wires, carrier diffusion lengths, and carrier lifetimes in GaAs/AlGaAs heterostructures

Thesis by

Hal Zarem

In Partial Fulfillment of the Requirements

for the Degree of

Doctor of Philosophy

California Institute of Technology

Pasadena, CA

1990

(Submitted November 22, 1989)

To my parents,

who always encouraged me to be inquisitive.

Acknowledgments

First I would like to thank my advisor, Amnon Yariv. He has created a very fertile and exciting research environment and I am proud to have been a part of it. I am especially appreciative of the freedom that he has allowed me throughout my graduate career. It has been very helpful in my development as a researcher.

Most of the work in this thesis has been done in collaboration with Kerry Vahala and other researchers in his group. From my perspective, this has been an extremely productive collaboration and I feel quite fortunate to have had so much interaction with him and his group.

Thanks are also due to Bill Bridges, with whom my brief but fruitful and enjoyable collaboration is the subject of Appendix A.

There have been many post-doctoral fellows, visiting researchers, students, and staff members who have helped me in the course of studies at Caltech. Let me start by mentioning those who have contributed directly to the work contained in this thesis: Pete Sercel, John Lebens, Lars Eng, Michael Hoenk, Steve Sanders, and Kent Nordstrom. Many others have been helpful with technical problems, research projects not contained in this thesis, and discussions on various topics in physics and other areas. These people include: Anders Larsson, Yasuhiko Arakawa, Josi Salzman, Joel Paslaski, Michael Mittelstein, Howard Chen, Ronnie Agranat, Dave Mehuys, Kaz Mitsunaga, Desmond Armstrong, Ali Ghaffari, and Jana Mercado.

One of the most special aspects of Caltech is the wonderful people that it attracts from all over the world. The friends I have made during the past five years have made

my time at Caltech more enjoyable as well as helped me to grow.

Special thanks go to my wife Lonnie for her unending support, encouragement, patience, and love.

I thank all of you very much.

Abstract

Nanometer scale wire structures are fabricated by selective disorder of a GaAs/AlGaAs quantum well. These structures are investigated by cathodoluminescence (CL). Spectrally resolved CL images of the structures as well as local CL spectra of the structures are presented. The effects of fabricational variations on quantum wire laser gain spectra and performance are discussed. A new technique for determining carrier diffusion lengths by cathodoluminescence measurements is presented. The technique is extremely accurate and can be applied to a variety of structures. The ambipolar diffusion length and carrier lifetime are measured in $\mathrm{Al_xGa_{1-x}As}$ for several mole fractions in the interval $0 < x < 0.38$. These parameters are found to have significantly higher values in the higher mole fraction samples. These increases are attributed to occupation of states in the indirect valleys, and supporting calculations are presented.

Contents

Chapter 1

Introduction

1.1 Semiconductor Devices

In the course of the past fifty years, semiconductor devices have been at the heart of many of the technological changes our society has undergone. Diodes, transistors, and digital logic circuits are in virtually every device or appliance that uses electricity. Computers and microprocessors serve functions that vary from setting the exposure in a camera, to controlling the course of remote spacecraft, to storing and processing most of the documents and data kept by businesses and individuals.

Early semiconductor research was centered on Ge. Because it has a lower melting point and was easier to purify than Si, the basic material properties and physics of Ge were uncovered sooner. In the late 1940's, the research on Ge led to the discovery of the transistor [1,2]. Because of the potential of the transistor in replacing the vacuum tube, research on transistors and semiconductors was greatly increased. For use as diodes and transistors, Si has come to replace Ge almost completely. This is due to a variety of reasons, such as: Si has a higher bandgap, allowing for higher operating temperatures for devices, the important fabrication processes of doping and oxide formation are easier in Si, and the raw material is less expensive. Although some researchers expected GaAs to be a replacement for Si in electronics because of its high electron mobility and saturation velocity, it is in the area of optoelectronics that GaAs has had the biggest impact.

An important difference between GaAs and Si or Ge is that GaAs is a direct gap semiconductor. This allows for the efficient conversion of electrical energy to light. Also, GaAs, being a compound semiconductor, can form a ternary compound with Al, $Al_xGa_{1-x}As$, where x is the Al mole fraction, that is, x represents the fraction of Ga sites that are occupied by an Al atom. The bandgap energy and index of refraction of $Al_xGa_{1-x}As$ change as x is varied, allowing a great degree of freedom in determining the electrical and optical properties of a device. It is fortunate that as the bandgap of $Al_xGa_{1-x}As$ increases, the refractive index decreases, making possible structures that confine both the optical field and the carriers to the same region. For the semiconductor laser, which relies on a significant overlap of the regions of high electron and hole concentration, and the optical field, this "accident of nature" is essential[1].

The first demonstrations of lasing in a semiconductor occurred in 1962 [3,4,5]. In the early devices, room temperature current densities were on the order of 5 x $10^4 A/cm^2$, and only pulsed operation was possible. Clearly, room temperature cw

---

[1] This "accident" occurs in any material where the refractive index change is governed by the Kramers-Kronig relation.

operation was required for these lasers to be useful. Through improvements in the material quality and laser design, researchers achieved room temperature cw operation by 1970. Since then semiconductor lasers have been used in fiber optic communication systems, retrieval of data stored on optical disks, and laser printers, to name a few of the current applications. One proposed future application for semiconductor lasers is optical interconnections for complex circuits in computers and other sophisticated electronic devices. Replacing metal strip lines with lasers and detectors has two basic advantages: first, lasers can be modulated at a high rate, speeding up communication between different elements of the circuit or system, and second, optical beams can intersect without interfering with each other, which increases the number of possible layouts on a circuit board. In this proposed application, thousands or tens of thousands of lasers would be utilized in one computer. For this to be feasible, each laser must have a threshold current in the low milliampere or microampere range. Recent efforts with quantum well lasers have pushed threshold current densities as low as 93A/cm^2 [6] and threshold currents down to 0.55mA [7] and there is promise of further reductions down to tens of microamperes.

1.2 Quantum Wells

One of the most important developments in semiconductor technology is the heterojunction. A heterojunction is the boundary between two different materials forming a single crystal. Electrons and holes traveling perpendicular to the heterojunction see a discontinuity in the bandgap at the heterointerface. With techniques such as molecular beam epitaxy (MBE) and organometallic chemical vapor deposition (OMCVD), these interfaces can be abrupt on the scale of a single atomic layer. In a double heterojunction structure, with a material of lower bandgap (e.g., GaAs) sandwiched between two layers of higher bandgap (e.g., $Al_xGa_{1-x}As$), electrons and holes become confined in the lower bandgap material.

The double heterostructure becomes a quantum well when the width of the confining structure is comparable to the deBroglie wavelength of the electron in the material. This situation is the semiconductor version of the quantum mechanical particle in a box. The electron wavefunctions are the superposition of a Bloch function and a standing wave envelope function consisting of two phase coherent, counterpropagating plane waves. This situation is illustrated in Fig. 1.1. Because the electron momentum in one direction is restricted to the eigenstates of the potential, it has only two degrees of freedom. Carriers in a quantum well are said to form a quasi-two-dimensional electron gas. In such a system, the density of states is step-like (see Fig. 1.2), as compared to the $\sqrt{E}$ dependence for the bulk case. Because the density of states increases abruptly from zero at the bottom of the first subband, no carriers are wasted in regions of the spectrum that lack a sufficient density of states to provide significant gain. The result of this is that a higher fraction of the carriers are contributing to the peak gain. When used as the active region of a laser, quantum well material yields lower threshold currents [7] and higher differential gain (leading to higher modulation bandwidths) [8,9], narrow linewidth [8,10], and reduced temperature dependence of the threshold current [11]. Quantum well active regions in lasers

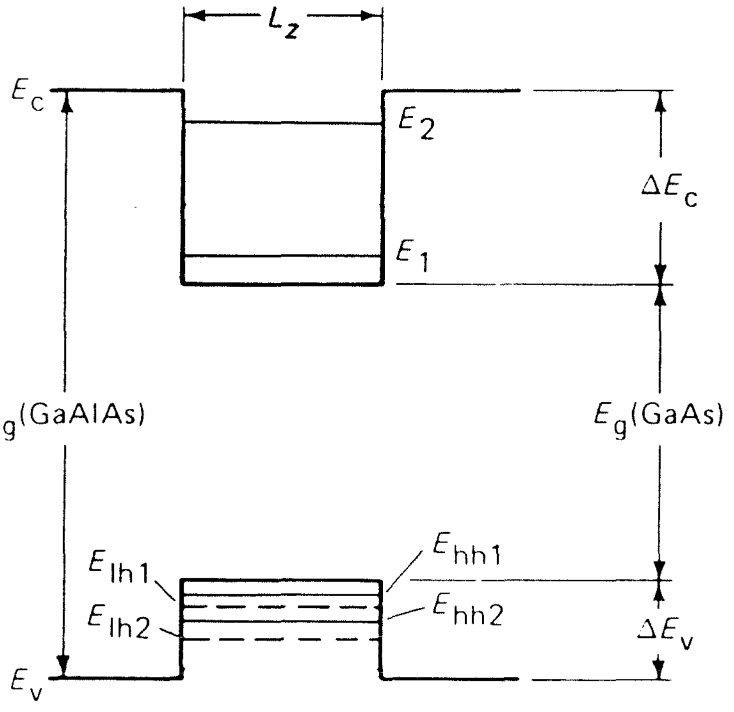

Figure 1.1: Band diagram for a quantum well. E_1 and E_2 are the eigenenergies for the first and second quantized state of the electron, and the E_{hh} and E_{lh} states represent the eigenenergies for the heavy hole and light hole respectively. Quantum wells in GaAs typically have layer thickness L_z in the range of 70-125Å.

have proved extremely successful and these lasers are now produced commercially for a variety of applications.

One interesting application for quantum well structures is as infrared photodetectors, where the absorption process is based on intersubband transitions of electrons in the conduction band, rather than on band to band transitions [12]. In these devices, electrons are placed in the lowest subband (E_1 in Fig. 1.1) by heavily doping the quantum well, and they are excited to a higher subband (E_2 in Fig. 1.1) or a continuum state by the infrared photons. The electrons are then swept from these higher states by a bias voltage, resulting in a photocurrent. By appropriate design of the quantum wells, you can tailor the absorption spectrum of the structure. Detectors that operate near 10μm, which coincides with an atmospheric spectral window, have been demonstrated [13], and could prove to be competitive with HgCdTe detectors in this wavelength range. These structures also show promise in the areas of optical computing [14] and second harmonic generation [15]. Recently, an infrared detector based on intersubband absorption and sequential resonant tunneling in a GaAs/AlGaAs superlattice has been demonstrated [16].

A device that is closely related to the quantum well is the double barrier tunneling structure. This electrical device, first demonstrated by Chang, Esaki, and Tsu [17], is of interest because of its negative differential resistance. When the Fermi energy of the injected carriers lines up with the subband energy in the quantum well, resonant tunneling occurs. This situation is analogous to the resonance that occurs with photons in a Fabry-Perot resonator. Resonant tunneling diodes have applications as multiple state memory cells [18], high speed logic devices [19], and millimeter wave oscillators [20], and have been operated in a detection experiment at frequencies as high as 2.5 THz [21].

When quantum wells were first proposed and demonstrated, there were doubts as to whether these devices could be fabricated well enough to realize the benefits of a confined structure. Now, it is clear that quantum well devices have real technological applications and are not restricted to laboratory demonstrations.

1.3 Quantum Wires and Quantum Boxes

Quantum wires and quantum boxes (sometimes called quantum dots) are the one and zero dimensional analogs of the quantum well. In these structures, the electron momentum is confined in one (for the wire) or two (for the box) of the lateral (in the plane of the substrate) dimensions as well as the vertical dimension. With the further reduction in dimensionality, the density of states becomes even sharper and narrower. This is illustrated in Fig. 1.2. Many of the advantages of quantum well lasers such as reduced threshold current, narrow linewidth, reduced temperature dependence of the threshold current, and high modulation bandwidth are related to the two-dimensional nature of the electrons in quantum wells, and theoretical investigations of one-dimensional or zero-dimensional structures have predicted further enhancements in many of these areas [8,11,22]. It is also possible that quantum wires and quantum boxes with their rich subband structures will create a host of new devices not yet conceived.

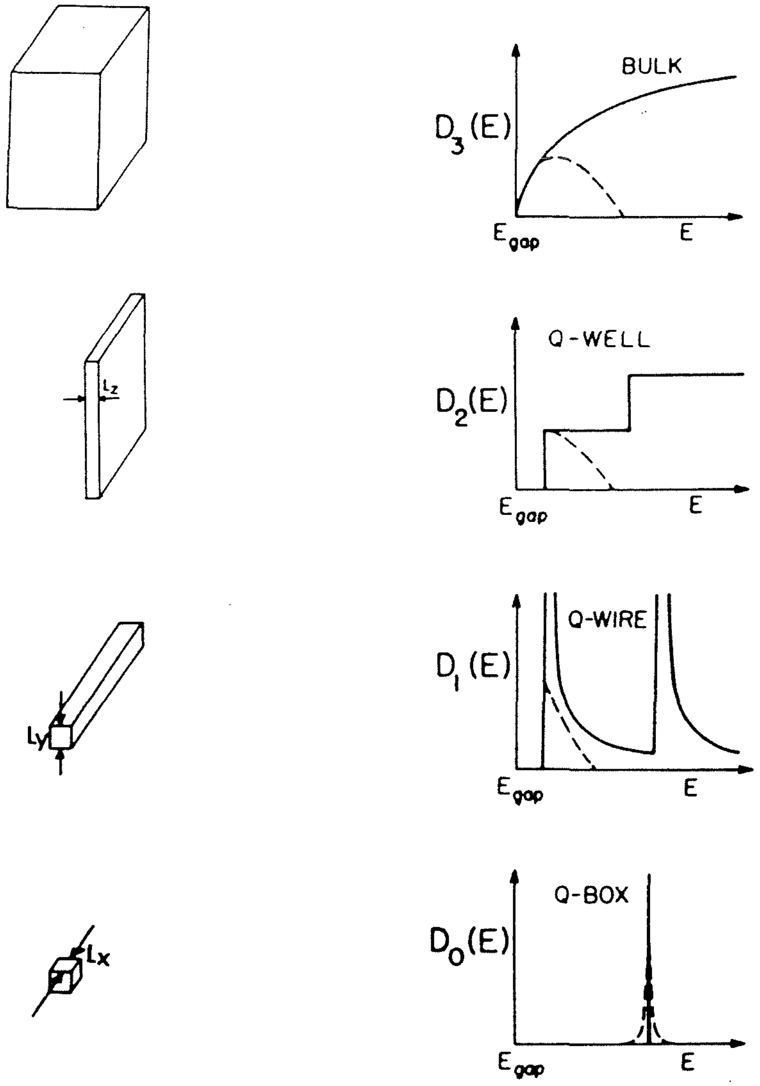

Figure 1.2: Illustration of the structure and density of states for a) bulk (three-dimensional), b) quantum well (two-dimensional), c) quantum wire (one-dimensional), and d) quantum box (zero-dimensional) material. The dashed curves represent gain spectra when these states are filled with carriers.

There have been several observations of quantum size effects in quantum wires and quantum boxes, but these structures have proven quite difficult to fabricate. To date, processing techniques have included etching of narrow ribbons and posts [23], ion implantation [24], growth of tilted superlattices [25], and growth on patterned substrates [26]. Quantum well structures in high magnetic fields have been used to simulate some of these effects [8,27]. As a result of these efforts there is much promise for quantum wire and quantum box lasers, but it is clear that significant work is still required before the full potential for these devices will be realized.

1.4 Outline of the Work Presented Here

The first half of what follows, Chapters 2 and 3, pertains to quantum wire fabrication. In Chapter 2, the effects of fabricational inhomogeneities on quantum wire gain spectra and quantum wire laser performance are examined. Although others have calculated gain spectra for these structures [28], the question of fabrication tolerance was previously neglected. Inhomogeneities will be much more significant for quantum wires and quantum boxes than for quantum wells. For quantum wells, confinement is provided by the heterojunction whose uniformity is good to one or two atomic layers, typically. In this case, the effects of inhomogeneous broadening are no greater than those of relaxation broadening, so inhomogeneities can be neglected. Most of the methods used or tried for fabricating quantum wires require some type of lithographic patterning and have lower fabrication tolerances than epitaxial techniques. Chapter 2 reexamines quantum wire gain spectra using realistic fabrication tolerances.

In Chapter 3, a new approach to fabricating quantum wires is demonstrated. With this method, a shallow Zn diffusion is used to selectively disorder a quantum well. The technique avoids the problems of free surfaces created by etching, and the damage created by ion implantation. The technique is only partially successful, in that, although we see evidence that is suggestive of quantum size effects due to the lateral confinement, there are other physically reasonable explanations for our results. We are able to conclude that carrier confinement on a nanometer scale has been created by this method.

A new method for determining carrier diffusion lengths by cathodoluminescence (CL) is presented in Chapter 4. This measurement technique is shown to be very accurate and straightforward. As compared with other approaches, the technique has the advantage that it requires minimal numerical analysis of the data, and no knowledge of other material parameters. This method is also interesting because it could be applied to quantum wire structures to study the effects of reduced dimensionality on diffusive transport. (There are predictions of increased mobilities in quantum wires [29].)

Although we do not measure diffusion lengths in quantum wires, we do apply this technique to ambipolar diffusion in $Al_xGa_{1-x}As$ for several values of x in the interval $0 \leq x \leq 0.37$ and find some interesting results. While the electron and hole mobilities are known to decrease with increasing x in this interval, the diffusion length is found to increase significantly for $x \geq 0.3$. This implies an increase in the carrier lifetime. To verify this, direct lifetime measurements are also performed by examining the photoluminescence signal decay under pulsed excitation. These data are presented in Chapter 5 along with calculations that indicate that the increased lifetime is due to the onset of carrier transfer and population of the indirect valleys at $x > 0.3$.

An experiment in holographic lithography that has possible applications for fabrication of quantum wires as well as distributed feedback lasers is included as Appendix A.

Chapter 4 and Chapter 5 represent a change in direction from that of the first three chapters, and some explanation for this is appropriate. In the course of the investigations of the wire structures described in Chapter 3 we found that the resolution limit of CL was determined by carrier diffusion. This is discussed in Section 3.2 and illustrated in the CL image of Fig. 3.5. It was our frustration with this limit, which drove us to devise a way to exploit it, that is, use it to measure carrier diffusion lengths. The success of the measurement and the interesting results that it uncovered indicate that it warranted significant time and attention.

Much of the work in this thesis has been published previously: the work of Ref. [30] is in Chapter 2, Chapter 3 details the work described in Ref. [31], and the work of Chapters 4 and 5 appears in Ref. [32] and Refs. [33] respectively. The results of Appendix A have been published in Ref. [34]. Although there are sections of this thesis that do not appear in any of these articles, everything described in these articles is contained in this thesis.

Bibliography

[1] J. Bardeen and W. H. Brattain, "The Transistor, A Semiconductor Triode," *Phys. Rev.*, **74**, 230 (1948).

[2] W. Shockley, "The Theory of p-n Junctions in Semiconductors and p-n Junction Transistors," *Bell Syst. Tech. J.*, **28**, 435 (1949).

[3] R. N. Hall, G. E. Fenner, T. J. Soltys, and R. O. Carlson, "Coherent Light Emission from a GaAs Junction," *Phys. Rev. Letts.* , **9**, 366 (1962).

[4] M. I. Nathan, W. P. Dumke, G. Burnes, F. H. Dills, and G. Lasher, "Stimulated Emission of Radiation from GaAs $p-n$ Junctions," *Appl. Phys. Letts.*, **1**, 62 (1962).

[5] T. M. Quist, R. J. Keyes, W. E. Krag, B. Lax, A. L. McWhorter, R. H. Rediker, and H. J. Zeigler, "Semiconductor Maser of GaAs," *Appl. Phys. Letts.*, **1**, 91 (1962).

[6] H. Z. Chen, A. Ghaffari, H. Morkoc, and A. Yariv, "Effect of substrate tilting on molecular beam epitaxial grown AlGaAs/GaAs lasers having very low threshold current densities," *Appl. Phys. Letts.*, **51**, 2094 (1987).

[7] K. Y. Lau, P. L. Derry, and A. Yariv, "Ultimate limit in low threshold quantum well GaAlAs semiconductor lasers," *Appl. Phys. Letts.*, **52**, 88 (1988).

[8] Y. Arakawa, K.Vahala, and A.Yariv, "Dynamic and Spectral Properties of Semiconductor Lasers With Quantum-Well and Quantum-Wire Effects," *Surf. Sci.*, **174**, 155 (1986).

[9] K. Uomi, T. Mishima, and N. Chinone, "Ultrahigh Relaxation Oscillation Frequency (up to 30GHz) of Highly P-Doped GaAs/GaAlAs Multiple Quantum Well Lasers," *Appl. Phys. Lett.*, **51**, 78 (1987).

[10] P. L. Derry, T. R. Chen, Y. H. Zhuang, J. Paslaski, M. Mittelstein, K. Vahala, and A. Yariv, "Spectral and Dynamic Characteristics of Buried Heterostructure Single Quantum Well (Al,Ga)As Lasers," *Appl. Phys. Lett.*, **53**, 271, (1988).

[11] Y. Arakawa and H. Sakaki, "Multidimensional quantum well laser and temperature dependence of threshold current," *Appl. Phys. Lett.*, **40**, 939 (1980).

[12] J. S. Smith, L. C. Chiu, S. Margalit, and A. Yariv, "A new infrared detector using electron emission from multiple quantum wells," *J. Vac. Sci. Technol. B*, **1**, 376 (1983).

[13] B. F. Levine, C. G. Bethea, G. Hasnain, J. Walker, and R. J. Malik, "High-detectivity $D^*=1.0x10^{10}cm\sqrt{Hz}/W$ GaAs/AlGaAs multiquantum well $\lambda = 8.3\mu m$ infrared detector," *Appl. Phys. Letts.*, **53**, 296 (1988).

[14] B. F. Levine, K. K. Choi, C. G. Bethea, J. Walker, and R. J. Malik, "GaAs Quantum Well Intersubband Absorption Tunneling Detectors Compatible with $10\mu m$

Optical Computing," *SPIE* **881** *Optical Computing and Nonlinear Materials*, 74 (1988).

[15] M. M. Fejer, S. J. B. Yoo, R. L. Byer, A. Harwit, and J. S. Harris, Jr., "Observation of Extremely Large Quadratic Susceptibility at 9.6-10.8μm in Electric-Field-Biased AlGaAs Quantum Wells," *Phys. Rev. Letts.*, **62**, 1041 (1989).

[16] B. F. Levine, K. K. Choi, C. G. Bethea, J. Walker, and R. J. Malik, "New 10 μm infrared detector using intersubband absorption in resonant tunneling GaAlAs superlattices," *Appl. Phys. Letts.*, **50**, 1092 (1987).

[17] L. L. Chang, L. Esaki, and R. Tsu, "Resonant Tunneling in Semiconductor Double Barriers," *Appl. Phys. Letts.*, **24**, 593 (1974).

[18] J. Soderstrom and T. Andersson, "A Multiple-State Memory Cell Based on the Resonant Tunneling Diode," *IEEE Electron Device Letts.*, **9**, 200 (1988).

[19] H. C. Liu and D. D. Coon, "Heterojunction double-barrier diodes for logic applications," *Appl. Phys. Letts.*, **50**, 1246 (1987).

[20] E. R. Brown, T. C. L. G. Sollner, W. D. Goodhue, and C. D. Parker, "Millimeter-band oscillations based on resonant tunneling in a double-barrier diode at room temperature," *Appl. Phys. Letts.*, **50**, 83 (1987).

[21] T. C. L. G. Solner, W. D. Goodhue, P. E. Tannenwald, C. D. Parker, and D. D. Peck, "Resonant tunneling through quantum wells at frequencies up to 2.5 THz," *Appl. Phys. Letts.*, **43**, 588 (1983).

[22] M. Asada, Y. Miyamoto, and Y. Suematsu, "Gain and the Threshold of Three-Dimensional Quantum-Box Lasers," *IEEE Journal of Quantum Electron.*, **QE-22**, 1915 (1986).

[23] K. Kash, A. Scherer, J. M. Worlock, H. G. Craighead, and M. C. Tamargo, "Optical Spectroscopy of Ultrasmall Structures Etched From Quantum Wells," *Appl. Phys. Lett.*, **49**, 1043 (1986).

[24] J. Cibert, P. M. Petroff, G. J. Dolan, A. C. Gossard, and J. H. English, "Optically Detected Carrier Confinement to One and Zero Dimension in GaAs Quantum Well Wires and Boxes," *Appl. Phys. Lett.*, **49**, 1275 (1986).

[25] M. Tsuchiya, J. M. Gaines, R. H. Yan, R. J. Simes, P. O. Holtz, L. A. Coldron, and P. M. Petroff, "Optical Anisotropy in a Quantum-Well-Wire Array with Two-Dimensional Quantum Confinement,"*Phys. Rev. Letts.*, **62**, 466 (1989).

[26] E. Kapon, D. M. Hwang, and R. Bhat, "Stimulated Emission in Semiconductor Quantum Wire Heterostructures,"*Phys. Rev. Letts*, **63**, 430 (1989).

[27] K. Vahala, Y. Arakawa, and A. Yariv, "Reduction of the Field Spectrum Linewidth of a Multiple Quantum Well Laser in a High Magnetic Field — Spectral Properties of Quantum Dot Lasers," *Appl. Phys. Lett.*, vol. 50, pp.365-367, (1987).

[28] M. Asada, Y. Miyamoto, and Y. Suematsu, "Theoretical Gain of Quantum-Well Wire Lasers," *Jpn. J. Appl. Phys.*, **24**, L95 (1985).

[29] H. Sakaki, "Scattering Suppression and High-Mobility Effect of Size-Quantized Electrons in Ultrafine Semiconductor Wire Structures," *Jpn. J. Appl. Phys.*, **19**, L735 (1980).

[30] Hal Zarem, Kerry Vahala, and Amnon Yariv, "Gain Spectra of Quantum Wires With Inhomogeneous Broadening," *J. Quantum Electron*, **QE-25**, 705 (1989).

[31] Hal A. Zarem, Peter C. Sercel, Michael E. Hoenk, John A. Lebens, and Kerry J. Vahala, "Nanometer scale wire structures fabricated by diffusion induced selective disordering of a GaAs(AlGaAs) quantum well," *Appl. Phys. Letts.*, **54**, 2692 (1989).

[32] H. A. Zarem, P. C. Sercel, J. A. Lebens, L. E. Eng, A. Yariv, and K. J. Vahala, "Direct determination of the ambipolar diffusion length in GaAs/AlGaAs heterostructures by cathodoluminescence," *Appl. Phys. Letts.*, **55**, 1647 (1989).

[33] H. A. Zarem, J. A. Lebens, K. B. Nordstrom, P. C. Sercel, S. Sanders, L. E. Eng, A. Yariv, and K. J. Vahala, "Effect of Al mole fraction on carrier diffusion lengths and lifetimes in $Al_xGa_{1-x}As$," *Appl. Phys. Letts.*, **55**, 2622 (1989).

[34] H. A. Zarem, M. E. Hoenk, W. B. Bridges, K. Vahala, and A. Yariv, "Generation of 1180$\mathring{A}$ Period Gratings With a Xe Ion Laser," *Electron. Letts.*, **24**, 1366 (1988).

Chapter 2

Gain Spectra of Quantum Wires With Inhomogeneous Broadening

2.1 Introduction

The technology used to fabricate quantum wells relies on growth techniques capable of atomic layer tolerances, leading to actual quantum well devices that exhibit nearly ideal properties. Confinement in directions other than the growth direction requires lithographic patterning and the best lithographic techniques have resolutions on the order of ten nanometers. Quantum size effects are extremely sensitive to the dimensions of the confining structure. For these reasons, it is important to consider the effects of fabricational inhomogeneities on quantum wire and quantum dot structures. Variations in the size and shape of quantum wires or quantum dots will smear some of the sharpness out of the density of states of these structures, reducing some of the benefits of lower dimensionality. Inhomogeneities in quantum boxes have been considered recently and it was found that quantum box arrays with realistic fabrication tolerances are not well suited to high gain applications, but they may make possible very low threshold current lasers and may lead to optical amplifiers with improved noise characteristics [1]. A critical radius, below which no bound states exist for the quantum box, was also shown.

In this chapter, we investigate the properties of quantum wires, in particular, the effects of inhomogeneities on the density of states function and on gain are examined. The inhomogeneities are treated as a perturbation to an ideal wire and the perturbation energy is calculated to first order. The density of states for an array of wires with different widths is calculated and is used to calculate the gain of such a structure. This is done for cylindrical wires of 50Å radius and 150Å radius with several different degrees of inhomogeneity. The properties of a quantum wire laser are examined and we attempt to answer the question of whether quantum wires with realistic fabrication tolerances can fulfill the expectations of lower threshold currents, and higher modulation rates. The finite barrier quantum wire is studied and a quasi-critical radius is established, below which, the carriers are weakly confined by the wire. Upper limits on the wire radius, determined by the requirement that the energy subbands be separated by an energy greater than $k_B T$, are also discussed.

2.2 Solution to the Two-Dimensional Finite Well Problem

A calculation of the electron and hole wave-functions is necessary to obtain the position of the energy subbands. Here we have treated the case of a cylindrical wire rather than the, somewhat simpler, rectangular wire employed elsewhere. This potential is chosen because the Schroedinger equation can be separated in the case of a finite cylindrical potential but not for a finite rectangular potential. A proper treatment of the finite potential is necessary to investigate the possibility of a critical radius below which no bound states exist. Such a critical radius has been shown to exist for the quantum box [1]. In this section we calculate the electron and hole wave-functions using the effective mass approximation. Their behavior as the radius of the wire goes to zero is examined.

In cylindrical coordinates the potential takes the simple form

$$V = V(\rho) = \begin{cases} 0 & \text{for } \rho < \rho_0 \\ V_0 & \text{for } \rho \geq \rho_0 \end{cases} \tag{2.1}$$

For this potential the Schroedinger equation is

$$-\frac{\hbar^2}{2m}\left(\frac{1}{\rho}\frac{\partial}{\partial\rho}\left(\rho\frac{\partial}{\partial\rho}\right) + \frac{1}{\rho^2}\frac{\partial^2}{\partial\phi^2} + \frac{\partial^2}{\partial z^2} + V(\rho)\right)\Psi(\rho,\phi,z) = E\Psi(\rho,\phi,z) \tag{2.2}$$

with solutions

$$\Psi(\rho,\phi,z) = N\begin{cases} J_\nu(k\rho)e^{i\nu\phi}e^{ik_z z} & \text{for } \rho < \rho_0 \\ AK_\nu(\kappa\rho)e^{i\nu\phi}e^{ik_z z} & \text{for } \rho \geq \rho_0 \end{cases} \tag{2.3}$$

where $J_\nu(k\rho)$ is the Bessel function of order $\nu = 0, \pm1, \pm2, \ldots$, and $K_\nu(\kappa\rho)$ is the modified Bessel function. The energy is given by

$$E = \frac{\hbar^2}{2m}(k_{\nu n}^2 + k_z^2) \tag{2.4}$$

The constants N, A, $k_{\nu n}$, and $\kappa_{\nu n}$ are determined by the normalization, the boundary condition at $\rho = \rho_0$, and the condition

$$k_{\nu n}^2 + \kappa_{\nu n}^2 = \frac{2m}{\hbar^2}V_0 \tag{2.5}$$

which follows directly from the Schroedinger equation. The radial momentum, $k_{\nu n}$, is a discrete variable whereas the axial momentum, k_z, varies continuously to fill the energy spectrum. In accordance with convention [2], $k_{\nu n}$ is the nth k-value to satisfy the boundary conditions for J_ν. In general there are an infinite number of k-values for each ν. In this treatment, only the first eight k-values are considered. This does not limit the validity of the analysis because only the first two or three subbands will be populated in realistic configurations.

There is no known way to solve for $k_{\nu n}$ analytically but for $V_0 \gg \hbar^2 k_{\nu n}^2/2m$, the boundary condition $J_\nu(k\rho_0) = 0$ applies approximately and the zeros of J_ν are tabulated [2]. As the radius of the wire becomes smaller, the subband energy is pushed up towards the top of the potential well and the above approximation is no longer valid. For small radius wires, the value of $k_{\nu n}$ can be obtained by expanding $J_\nu(k\rho)$ and $K_\nu(\kappa\rho)$ about the origin. The small argument expansions for J_0 and K_0 are given by,

$$J_0 = 1 - \frac{1}{4}(k\rho)^2 + \ldots \tag{2.5a}$$

$$K_0 = -\ln \kappa\rho + \ldots \tag{2.5b}$$

We use this to investigate the behavior of the ground state as the wire diameter approaches zero. Applying continuity at $\rho = \rho_0$ gives,

$$k\rho_0 = \left[\frac{2}{\frac{1}{2} - \ln \kappa\rho_0}\right]^{\frac{1}{2}} \tag{2.7}$$

Equations 2.6 and 2.4 are plotted in Fig. 2.1. The intersection of the two curves gives the eigenvalues for k and κ. It appears that Eq. 2.6 intersects the y-axis at $k\rho \approx \frac{1}{2}$, but, in fact, it has finite slope until it intersects the origin. As ρ_0 approaches

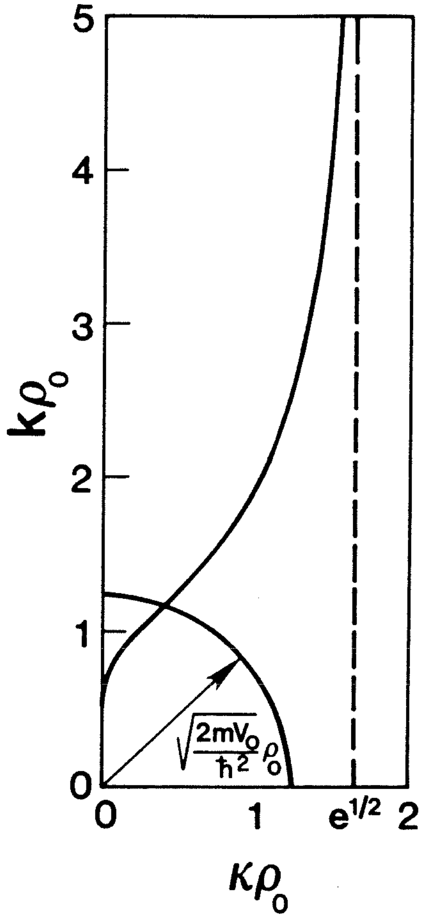

Figure 2.1: Graphical solution of the eigenvalue equation for the cylindrical potential. As the radius of the wire is reduced, the intersection moves toward the origin.

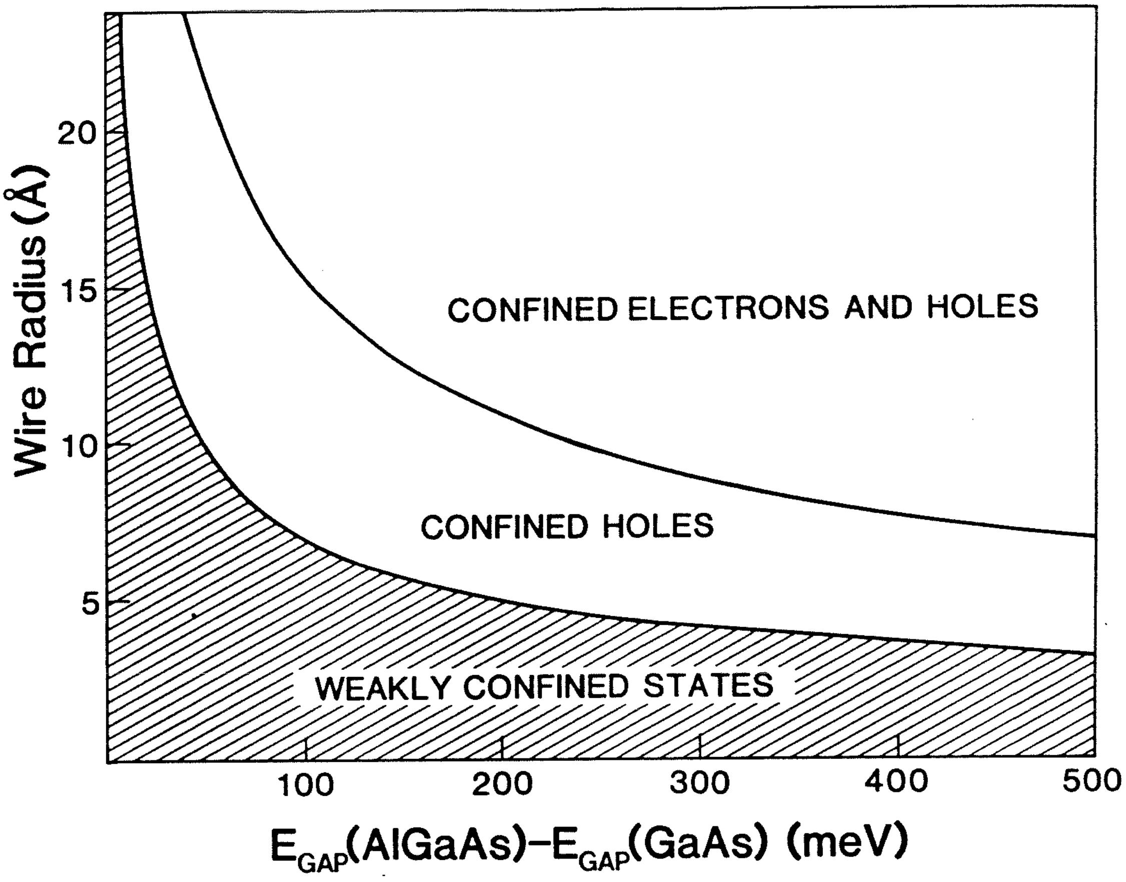

Figure 2.2: Quasi-critical radius as a function of the bandgap discontinuity. Electrons and holes in quantum wires that are smaller than the quasi-critical radius, are bound by the potential but are only weakly confined by it.

zero, the radius of the circle goes to zero and it is clear that there is always a bound state for the cylindrical potential. However, from Fig. 2.1 we see that when the radius of the circle is less than $\frac{1}{2}$, κ becomes small, indicating a weakly bound state. At this point it becomes improbable that the carrier remains in the wire. From this we define a quasi-critical radius,

$$\rho_c = \frac{1}{2}\sqrt{\frac{\hbar^2}{2mV_0}}, \tag{2.8}$$

below which the electron or hole is very weakly confined. Equation 2.7 is plotted in Fig. 2.2 as a function of V_0. We have assumed effective masses of $0.067m_0$ for electrons and $0.45m_0$ for heavy holes. The conduction band offset was taken as 60 percent of the band-gap discontinuity. Due to the large difference in their effective masses, there are regions where the holes are confined by the potential but the electrons are not. In the GaAs/AlGaAs system, the region of weakly confined states may occur only in structures as small as 5 – 10Å in radius. At this point, the effective mass approximation may give only qualitative features. For quantum boxes, there exists a strict critical radius below which no bound states exist [1]. The quasi-critical radius for quantum wires is a factor of π smaller than the critical radius for quantum boxes.

2.3 Roughened Cylinders

In this section we treat the case of an imperfect quantum wire. The wire is taken to have hard boundaries with a potential step equal to V_0 but the potential is no longer a function only of ρ_0, but of all three coordinates as in Fig. 2.3. We assume that the wire is close enough to cylindrical that the roughness may be treated as a

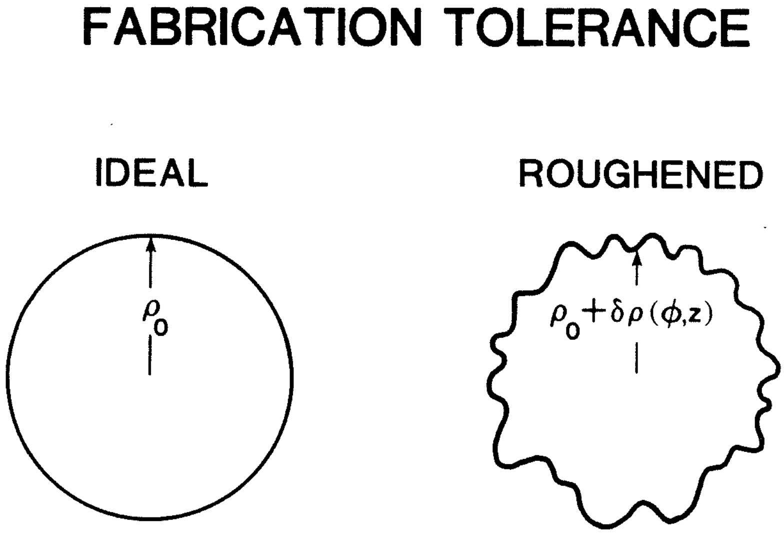

Figure 2.3: The cross section of an ideal and a roughened quantum wire.

perturbation of the potential $V(\rho)$ in the form,

$$W(\rho,\phi,z) = \begin{cases} -V_0 & \text{for } \rho_0 < \rho \leq \rho_0 + \delta\rho(\phi,z) \\ 0 & otherwise \end{cases} \tag{2.9}$$

where $\delta\rho(\phi,z)$ is an arbitrary, nonnegative function of ϕ and z whose magnitude is much less than ρ_0. We further require that $\delta\rho$ vary on a scale that is smaller than the coherence distance of the electron. With this perturbation, the average radius of the cylinder is increased by an amount $< \delta\rho(\phi,z) >_{\phi,z}$ where $<>_{\phi,z}$ denotes a spatial average over the coordinates ϕ and z. It is straightforward to show that application of first order perturbation theory to the ground state gives,

$$< \delta E > \equiv < \Psi_0 \mid W \mid \Psi_0 > = V_0 C^2 J_0(\kappa\rho_0)\rho_0 < \delta\rho(\phi,z) >_{\phi,z} \tag{2.9a}$$

$$C^2 = \left[\frac{1}{2}\rho_0^2 J_1^2(x_{01})\right]^{-1} \tag{2.9b}$$

where C^2 comes from the normalization of the Bessel function. In the limit as V_0 goes to infinity, Eq. 2.9 becomes

$$< \delta E > = -2\frac{< \delta\rho >_{\phi,z}}{\rho_0} E_{01} \tag{2.11}$$

where,

$$E_{01} = \frac{k_{01}^2 \hbar^2}{2m} = \frac{x_{01}^2 \hbar^2}{2m\rho_0^2} \tag{2.12}$$

is the energy of the first subband for the infinite barrier cylinder. To first order, the effect of the roughness is only through a change in the average radius. This implies that, to first order, quantum wires are insensitive to inhomogeneities that do not affect the average radius of the structure. Therefore, a fabrication tolerance of ten angstroms may be quite acceptable if the average radius does not change by more than a few angstroms from wire to wire. This does not apply if the perturbation varies with z on a scale that is large compared to the coherence length of the electron. Sections of the wire which are at least one coherence length apart can be considered as separate wires so that the averaging of $\delta\rho$ should be done for $z_0 < z < z_0 + l_c$ where l_c is the coherence length of the electron. If we assume an intraband scattering time of $2\text{x}10^{-13}s$ [3] and thermal velocity, l_c is on the order of 800Å at room temperature.

Equations 2.10 and 2.11 are general results in that they can be shown to hold for quantum wells and quantum boxes as well (with x_{01}^2 replaced by the appropriate value for wells or boxes) [1]. In the case of wells and boxes the confinement energy, E_{10}, is different, however. The confinement energy increases as the number of confined dimensions increases. For this reason, inhomogeneities will affect quantum boxes more severely than quantum wires and, likewise, quantum wires more severely than quantum wells. As the size of the structure is increased the confinement energy decreases, reducing the effect of inhomogeneities. The size can be increased only so far because the subbands must be separated by an energy that is greater than a few k_BT for quantum size effects to be realized. For all three low-dimensionality structures, the subband energy has a ρ^{-2} dependence. If we define ΔE as the separation between the first and second subbands, we can calculate the proportionality constant between ΔE and ρ^{-2}. The results are shown in Table 2.1 where ΔE is calculated for several values of ρ with $V_0 = \infty$, and using a spherical potential for the quantum box and a cylindrical potential for the quantum wire. In Table 2.1 and all of the figures and calculations here, values of constants that are appropriate for GaAs are chosen.

ΔE (meV)

		Well	Wire	Box
$\rho=\rho_0$		$(7.4)\frac{\hbar^2}{2m\rho_0^2}$	$(8.9)\frac{\hbar^2}{2m\rho_0^2}$	$(10.3)\frac{\hbar^2}{2m\rho_0^2}$
$\rho=50$Å	cb	168	202	234
	vb	25	30	35
$\rho=100$Å	cb	42	51	59
	vb	6.2	7.6	8.8
$\rho=200$Å	cb	11	13	15
	vb	1.6	1.9	2.2

cb=conduction band
vb=valence band

Table 2.1: The separation of the first and second subbands for different size quantum wells, quantum wires, and quantum boxes in GaAs. The parameter ρ is the radius, or, in then case of quantum wells, a half width. When ΔE is smaller than k_BT, thermal broadening smears out quantum size effects.

From Eq. 2.11 we see that a small change in radius $d\rho$ gives a change in subband energy

$$dE_{01} = -2\frac{d\rho}{\rho_0}E_{01} \tag{2.13}$$

which is the same as the result from the perturbation calculation. Comparing Eqs. 2.10 and 2.12 we see that the effect on the subband energy of roughening the cylinders with an average roughness $< \delta\rho >_{\phi,z}$ is equivalent to changing the wire width by $d\rho =< \delta\rho >_{\phi,z}$. It should be noted that Eq. 2.12 is an upper limit because it applies for the case of an infinite barrier; the finite barrier case will produce a smaller shift because of the softer boundaries. In what follows we assume that we have an ensemble of wires with different values of $< \delta\rho >_{\phi,z}$. In accordance with the central limit theorem we assume a Gaussian distribution of wire radii

$$P(\rho) = \frac{1}{\sqrt{2\pi}\delta\rho}\exp\left[\frac{-(\rho-\rho_0)^2}{\delta\rho^2}\right] \tag{2.14}$$

where ρ_0 is the average wire radius and $\delta\rho$ is the standard deviation of $< \delta\rho >_{\phi,z}$. The length of a typical semi-conductor laser is several hundred times the coherence length of the electron so the gain of a single wire must be obtained by considering the gain of many wires each of length l_c.

2.4 Gain Spectra

The density of states for an ideal (unroughened) wire of radius ρ_0 is,

$$D(E) = \sum_{l=1}^{\infty}\frac{(m_r/2\hbar^2)^{1/2}}{\pi^2\rho_0^2}(E - E_g - E_l)^{-1/2}\eta_l \tag{2.15}$$

where E is the energy of the transition, E_g is the band-gap, E_l is the position of the l^{th} subband (the index l is a combination of the indices n and ν of the previous sections), η_l is the degeneracy of the l^{th} subband ($\eta_l = 1$ for $\nu = 0$, $\eta_l = 2$ otherwise) and $m_r = m_e m_h/(m_e + m_h)$ where m_e and m_h are the masses of the electron and the hole respectively. Equation 2.14 is plotted in Fig. 2.4. In Fig. 2.4 and all subsequent figures, values of the material parameters that are appropriate for GaAs are used. These values are: $m_e = 0.067, m_h = 0.45, E_g = 1.424$. The subband positions, E_l, are calculated assuming an infinite bandgap discontinuity.

Changing the radius of a wire will affect the gain by moving the subband edge. We obtain a Gaussian distribution of subband energies by combining Eqs. 2.12 and 2.13

$$P(E_l) = \frac{1}{\sqrt{2\pi}\delta E_l} \exp\left[\frac{-(E_l - \overline{E_l})^2}{\delta E_l^2}\right] \tag{2.16}$$

where δE_l and E_l are related to $\delta\rho$ and ρ through Eqs. 2.10 and 2.11. The bulk density of states for the material is found by integrating Eq. 2.14 over all values of E_l weighted by equation 2.15 giving the inhomogeneous density of states,

$$D_{inh}(E) = \sum_{l=1}^{\infty} \frac{1}{\delta E_l \sqrt{2\pi}} \left(\frac{m_r}{2}\right)^{1/2} \frac{\eta_l}{\pi \rho_0^2 \hbar} \int (E - E_g - E_l)^{-1/2} \exp\left[\frac{-(E_l - \overline{E_l})^2}{\delta E_l^2}\right] dE_l \tag{2.17}$$

The integral in Eq. 2.16 is evaluated numerically and the inhomogeneous density of states is plotted for wires of radius $\rho = 50$Å in Fig. 2.5. The effects of the inhomogeneities are quite dramatic: for $\delta\rho = 2.5$Å, which corresponds to a mono-layer variation in radius, the subbands are distinct and the density of states recalls the basic features of the ideal density of states of Fig. 2.4, whereas, for $\delta\rho = 10$Å all subband

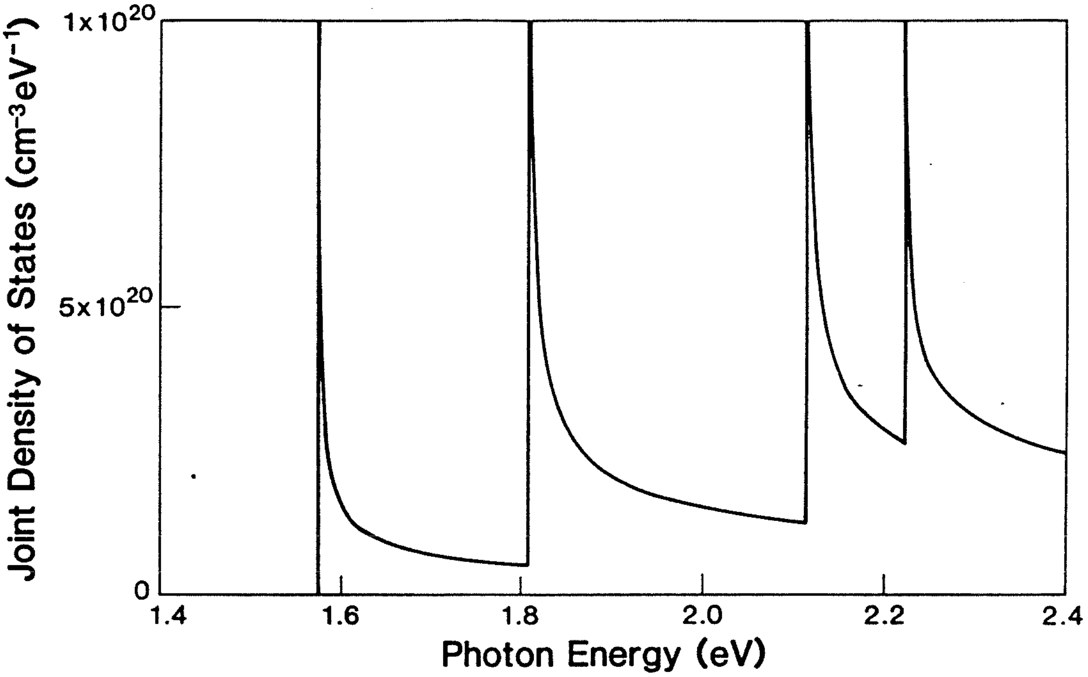

Figure 2.4: The density of states for 50Å radius quantum wires without inhomogeneous broadening.

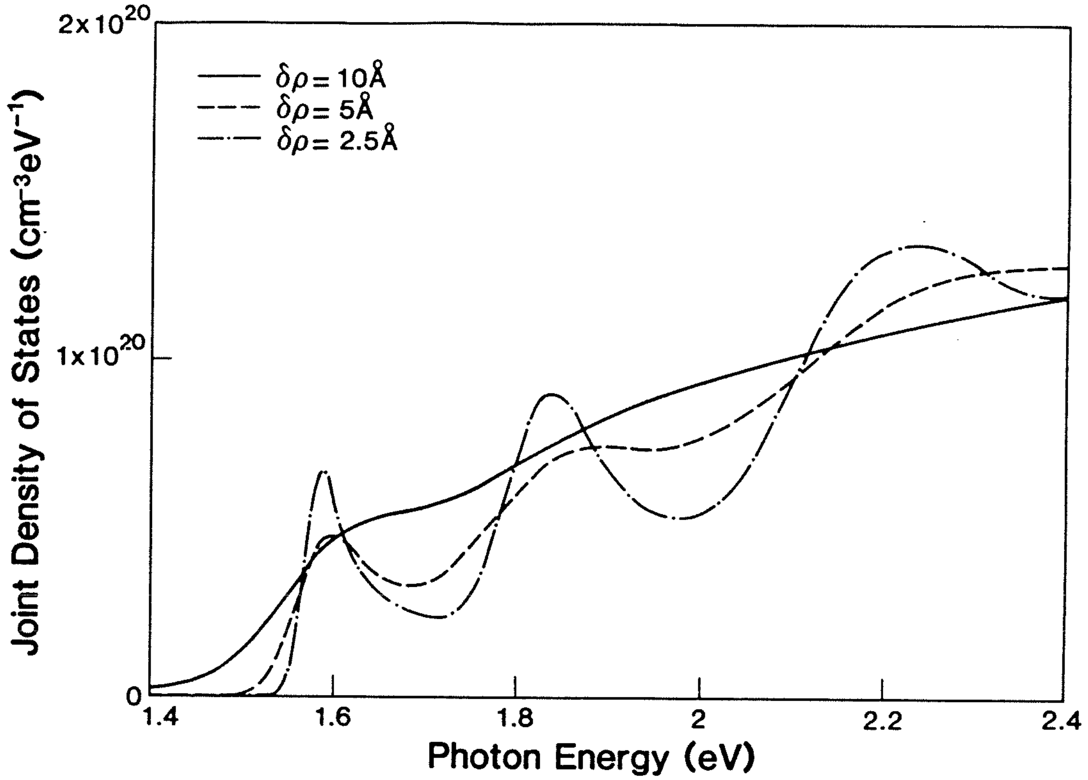

Figure 2.5: The density of states for 50Å radius quantum wires with three different values of the roughness parameter; $\delta\rho = 2.5$Å, $\delta\rho = 5.0$Å, and $\delta\rho = 10.0$Å.

structure is washed out and the density of states resembles that of bulk material. As the subbands broaden, their peak value decreases because the area under each curve must be the same. Fig. 2.6 shows the density of states for 150Å radius wires. The magnitude of the density of states is reduced by a factor of three as compared with 50Å wires. In general, the magnitude of the density of states will be inversely proportional to the radius of the wire if $\delta\rho/\rho$ is kept fixed (this follows directly from Eq. 2.16 when the dependence of E_l and δE_l on ρ_0 is considered). The shape of these curves is the same as that of a 50Å wire with the same value of $\delta\rho/\rho$ except that the energy scale is different due to the different subband positions. For $\delta\rho = 150$Å the first and second subband are separated by only 18meV. This means that at room temperature there will be substantial filling of the second subband when the first subband is partially filled, leading to increased threshold currents.

The density of states calculations shown in Figs. 2.5 and 2.6 are the basis of the gain calculations to follow. The broadening caused by the inhomogeneities is, in all cases considered here, greater than or equal to relaxation broadening. The gain is therefore given by,

$$G(E) = \frac{E}{\hbar}\sqrt{\mu/\epsilon} \mid d \mid^2 D(E)(f_c - f_v) \tag{2.18}$$

where ϵ is the dielectric constant of the material, μ is the magnetic susceptibility, f_c and f_v are the Fermi distributions for the conduction and valence bands respectively, and d is the component of the dipole moment parallel to the electric field. A value of $d/q = 4$Å has been assumed and any dependence of d on the orientation of the electric field with respect to the wire axis is ignored. The light hole band has also

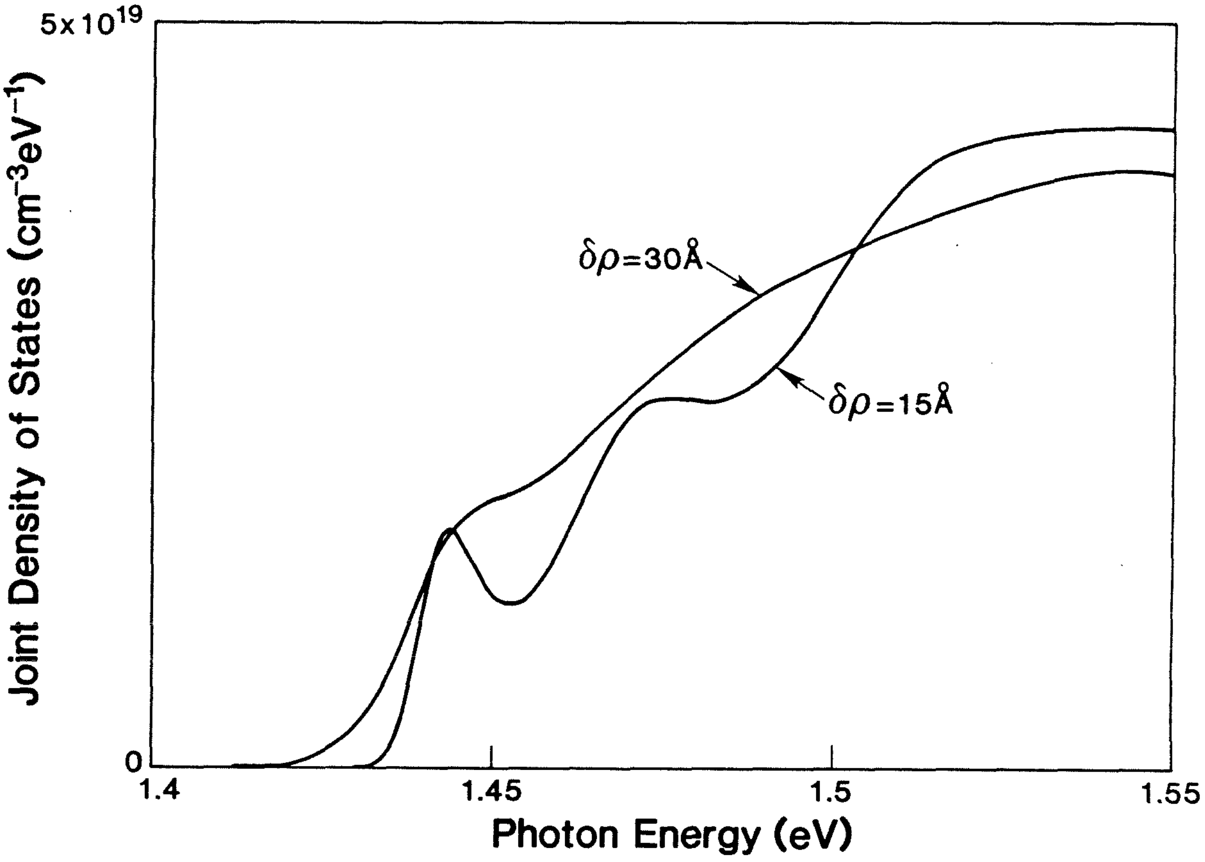

Figure 2.6: The density of states for 150Å radius quantum wires with two different values of the roughness parameter; $\delta\rho = 15$Å, and $\delta\rho = 30$Å.

been ignored in the calculation. The overlap of the field with the gain region is not yet accounted for in these plots so that $G(E)$ is the gain a wave would experience if it were fully confined to the quantum wire. The gain spectrum for a 50Å radius wire has been plotted in Fig. 2.7 for carrier densities of $4\text{x}10^{18}\text{cm}^{-3}$ and $8\text{x}10^{18}\text{cm}^{-3}$. As the carrier density is doubled, the peak gain increases almost proportionally, indicating that, even at this high carrier density, the carriers are going predominantly into the first subband. In Fig. 2.8 gain is calculated for the density of states functions of Fig. 2.5, showing the effects of increased inhomogeneities on the gain spectrum. All of the curves are for the same carrier density. Here, the benefits of a sharp density of states function are clear as the peak gain drops by roughly a factor of two when $\delta\rho$ goes from 2.5Å to 10Å. Fig. 2.9 shows the dependence of peak gain on carrier density for these same wires. The gain rises steeply at first, but it begins to level off at around $7\text{x}10^{18}\text{cm}^{-3}$ as the first subband becomes full. At a carrier density of roughly $1.3\text{x}10^{19}\text{cm}^{-3}$ the gain begins to rise sharply once again. It is at this point that the gain of the second subband exceeds that of the first. This has been observed experimentally in quantum well lasers [4] and it is accompanied by a large change in lasing wavelength. Curves similar to those of Figs. 2.8 and 2.9 but for 150Å radius wires are shown in Figs. 2.10 and 2.11. For any given carrier density, the gain of a 150Å wire is lower than that of a 50Å wire. This is due to two factors: first, the density of states is smaller for larger wires, and second, the subbands are separated by an energy that is less than k_BT, so several subbands are being filled simultaneously. Peak gain versus carrier density for the 150Å radius wires is plotted in Fig. 2.11.

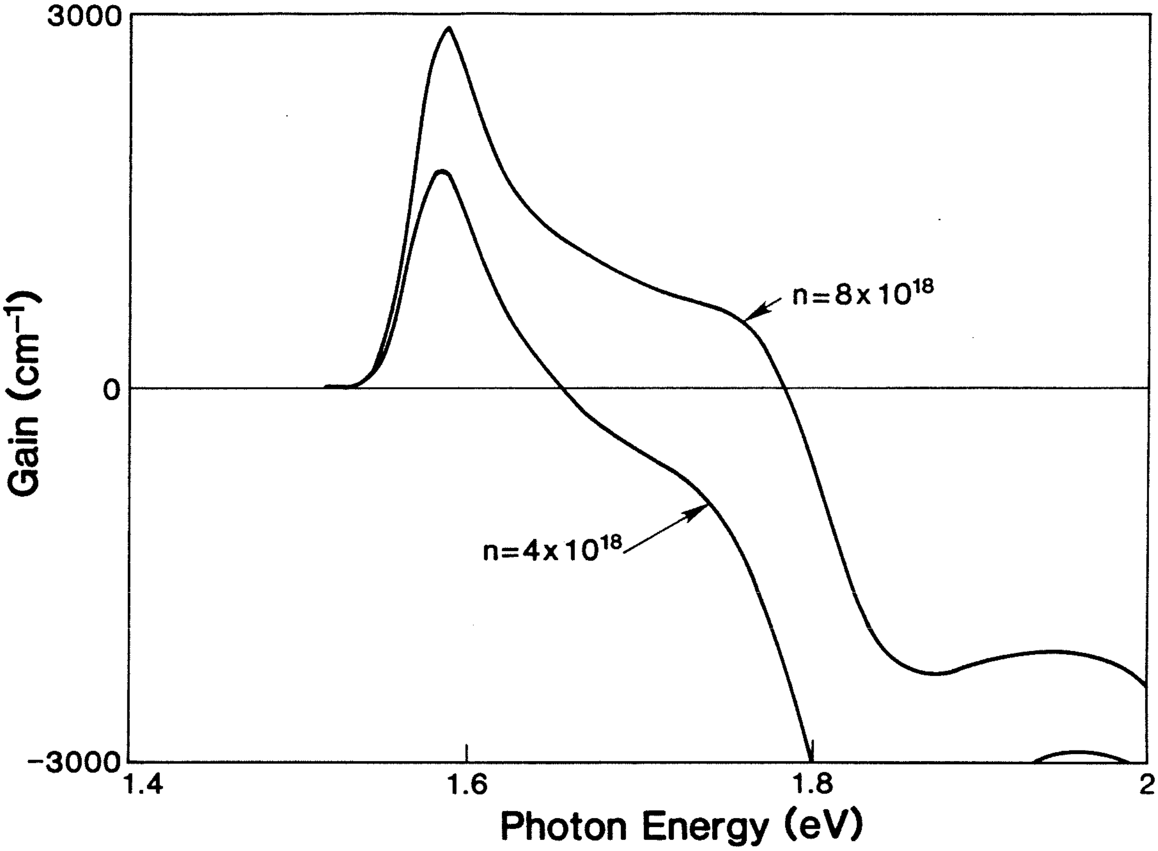

Figure 2.7: Gain as a function of photon energy for 50Å radius quantum wires with $\delta\rho = 2.5$Å at a carrier concentration of 4x10^{18}cm^{-3} and 8x10^{18}cm^{-3}.

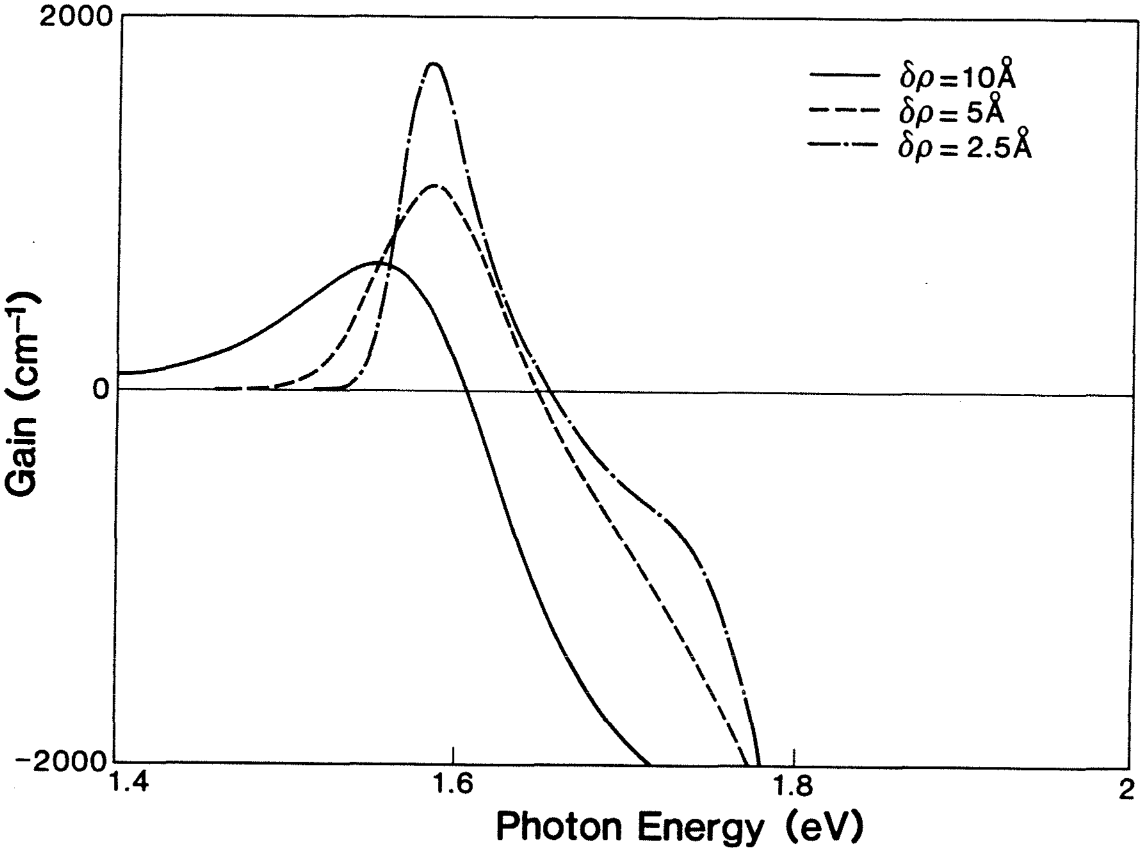

Figure 2.8: Gain as a function of photon energy for 50Å radius quantum wires with $\delta\rho = 2.5$Å, $\delta\rho = 5.0$Å, and $\delta\rho = 10.0$Å at a carrier concentration of 4x10^{18}cm^{-3}.

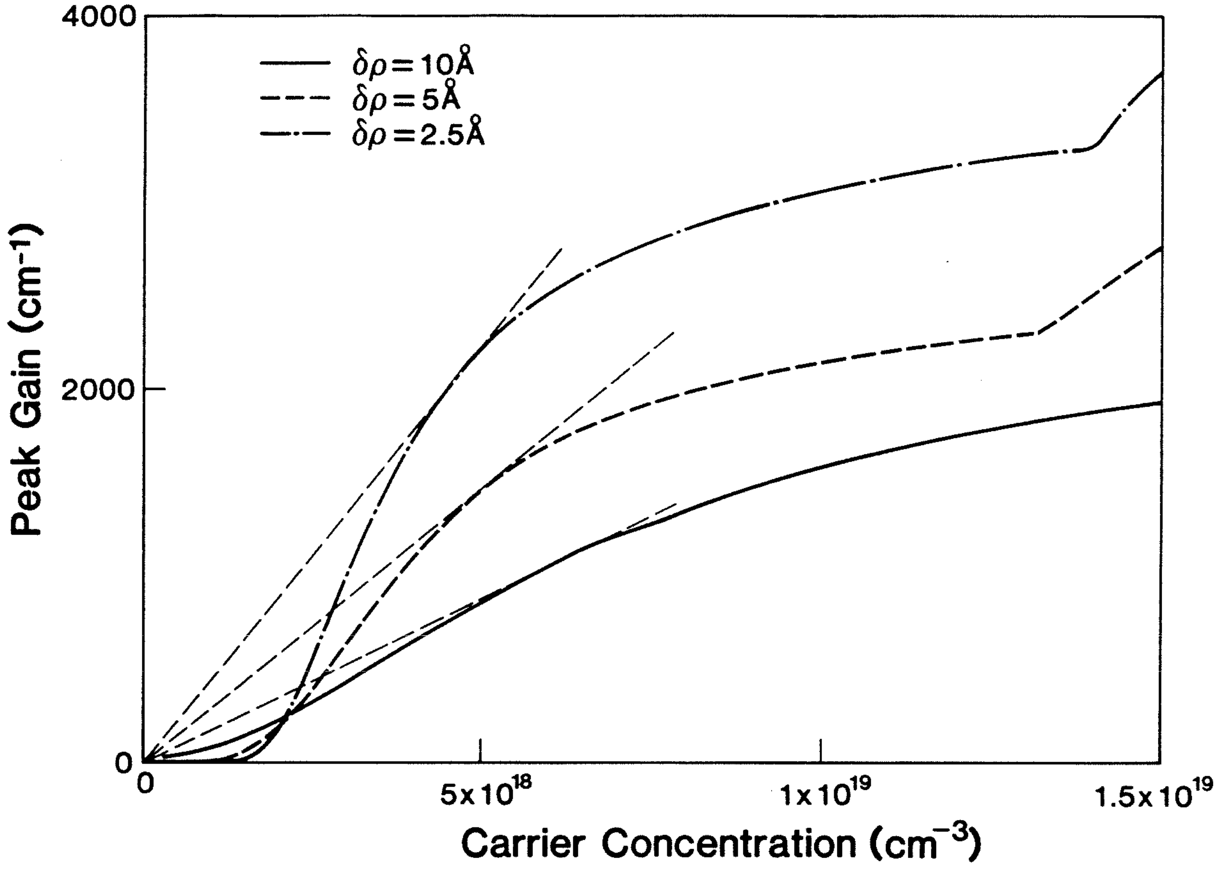

Figure 2.9: Peak gain as a function of carrier concentration for the quantum wires of Fig. 2.5. The sudden change in slope at high carrier densities is indicative of second quantized state lasing. The point of maximum gain per carrier density is given by the dashed tangent.

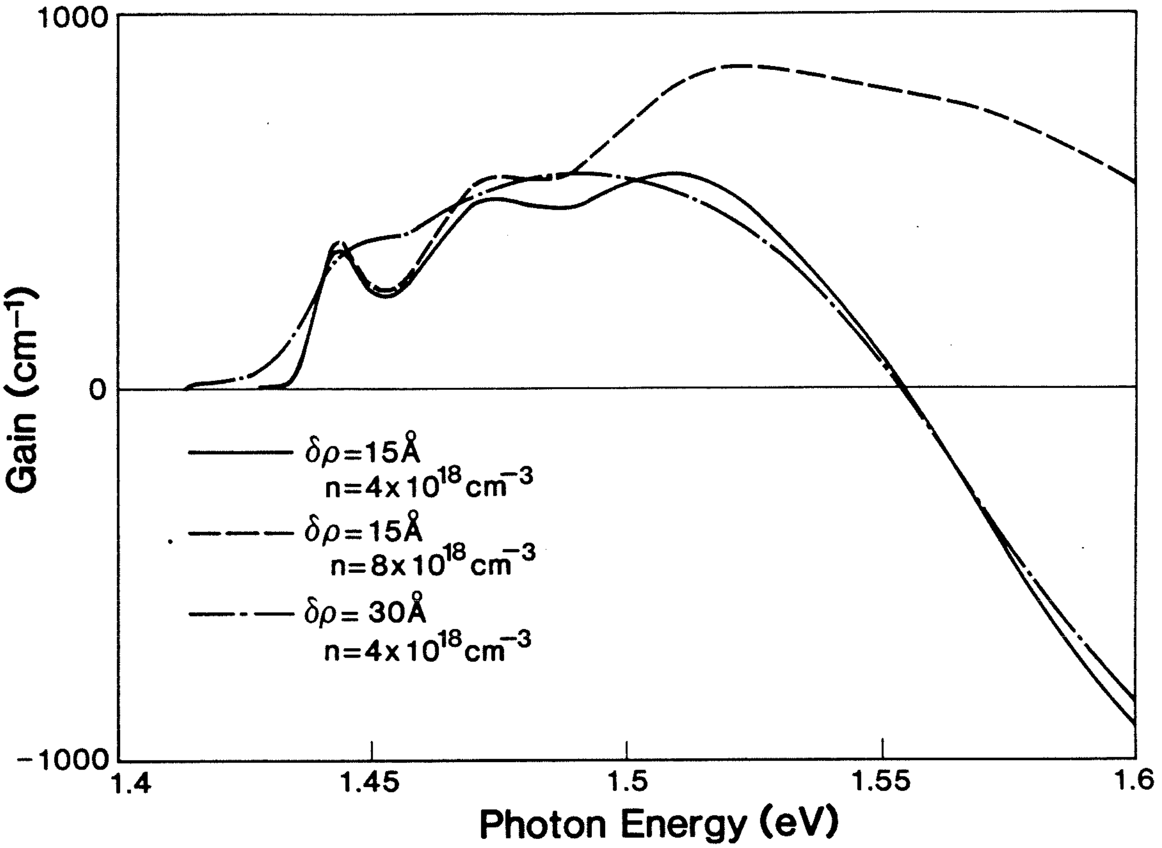

Figure 2.10: Gain as a function of photon energy for 150Å radius quantum wires with $\delta\rho = 15$Å, $\delta\rho = 30$Å, at a carrier concentration of 4x10^{18}cm^{-3}, and 150Å radius quantum wires with $\delta\rho = 15$Å at a carrier concentration of 4x10^{18}cm^{-3}.

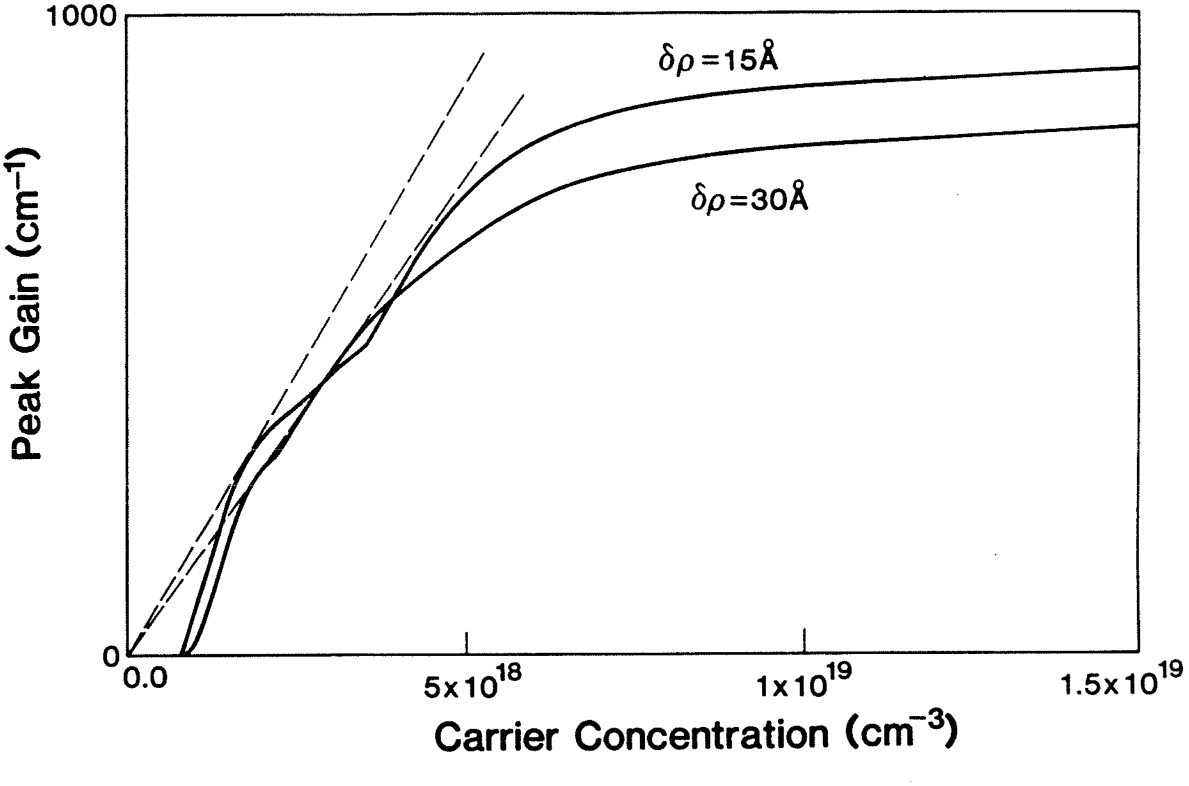

Figure 2.11: Peak gain as a function of carrier concentration for the quantum wires of Fig. 2.6. The point of maximum gain per carrier density is given by the dashed tangent.

2.5 Lasing Properties

So far, we have discussed the properties of quantum wires without considering the device in which they are to be imbedded. In this section we consider the modal gain, threshold current, and the modulation rate for a quantum wire laser. Figure 2.12 shows a schematic diagram of a quantum wire array laser. The dashed cylinder which envelops the quantum wires represents the optical confinement region and the width of the optical mode in the x and y directions is shown as W_x and W_y.

The modal gain is obtained by multiplying the bulk gain for a wire by the confinement factor, which is a measure of the overlap of the optical field with the gain region. Switching to rectangular coordinates and keeping the cylinder axis as the z-axis, the confinement factor is a product of confinement factors for the x and y directions, Γ_x and Γ_y. For a single wire of 50Å radius, $\Gamma_x = \Gamma_y = 0.04$ is a reasonable value [5]. If we take a peak gain of 3000cm^{-1} and the above confinement factors, the peak modal gain is $G_{mode} = 4.8\text{cm}^{-1}$ per wire. This is marginally sufficient gain to overcome the distributed losses so that to obtain additional gain to make up for mirror and coupling losses, we must employ an array of such quantum wires to make a laser.

The threshold gain is given by,

$$G_{modal,th} = \alpha - \frac{1}{l}\ln R \tag{2.19}$$

where α is the distributed loss coefficient for the mode, l is the length of the cavity, and R is the reflectivity of the mirrors. To estimate threshold current densities we assume values of $\alpha = 3\text{cm}^{-1}$, $l = 300\mu m$, and $R = 0.9$. For these values, $G_{modal,th} = 6.5\text{cm}^{-1}$.

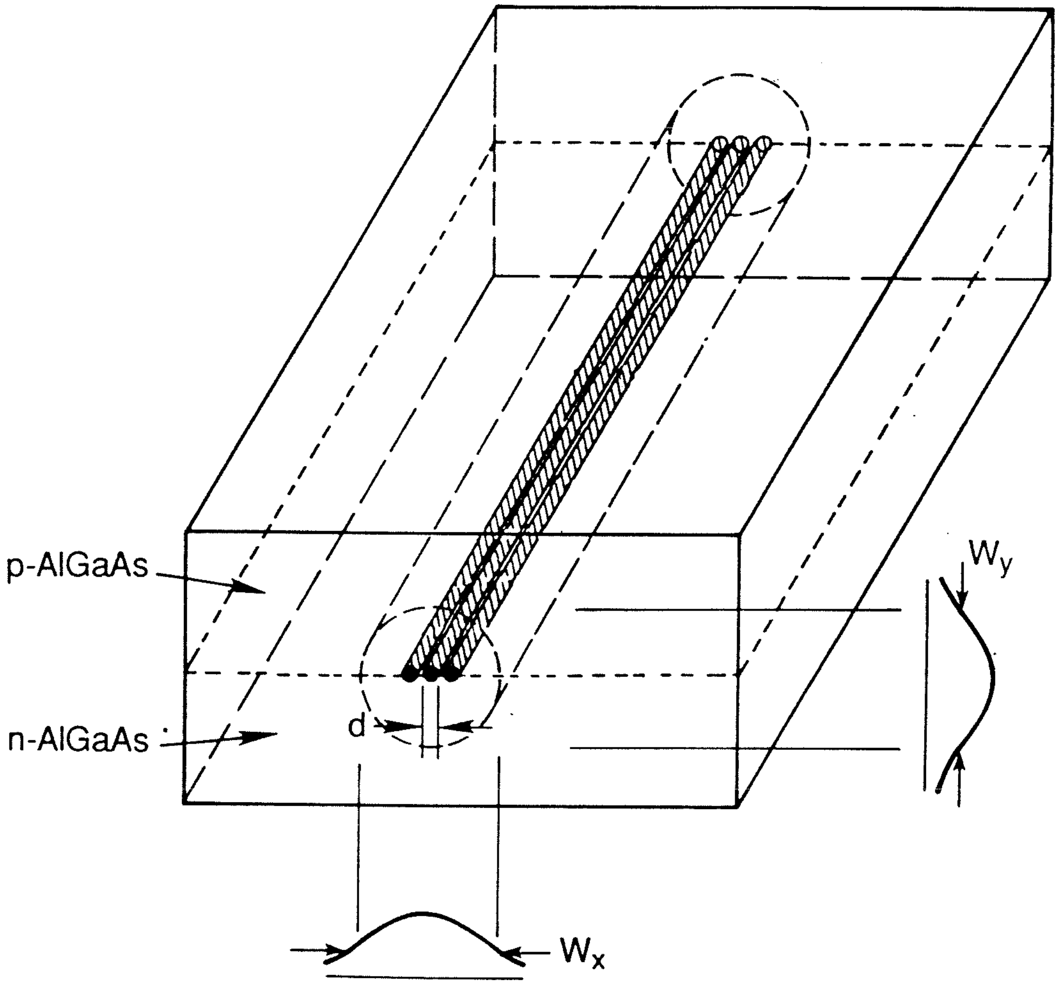

Figure 2.12: A Schematic of a quantum wire array laser. The width of the optical mode is given by W_x and W_y and the wire diameter is d. The confinement factor is given by the relation $\Gamma_i = d/W_i$.

To achieve the lowest threshold current, we want to pump the wires to the point of maximum gain per carrier density. This is the point on the peak gain vs. carrier density curve whose tangent intersects the origin. From Fig. 2.11, we see that this occurs at a carrier density of approximately 5x10^{18}cm^{-3} for a 50Å radius wire with $\delta\rho = 2.5$Å. At this point, the gain in the wire is approximately 2250cm^{-1}. With the above confinement factors, a laser with two such wires would have a modal gain of 7.2cm^{-1}, which is just above the estimated threshold gain. To arrive at a threshold current, a value of the carrier lifetime must be assumed. The effect of the two-dimensional confinement on the carrier lifetime is not known, so the bulk carrier lifetime is used. If we assume a carrier lifetime of $3ns$ [6], and 100 percent injection efficiency, this two-wire laser would have a threshold current of approximately $11\mu A$, which is nearly two orders of magnitude lower than the best quantum well lasers. When the same considerations are applied to a 50Å wire with $\delta\rho = 10$Å, the optimal carrier density is approximately 6.5x10^{18}cm^{-3}, and a laser containing four such wires would have a threshold current of approximately $33\mu A$, which is still extremely low. In the case of 150Å radius wires, the confinement factors increase to $\Gamma_x = \Gamma_y = 0.12$. Working backwards, if we assume a modal gain of 6.5cm^{-1} and the above confinement factors, the bulk gain requirement is only 450cm^{-1}. One wire can provide this gain and, under the same assumptions as above, the estimated threshold current is $34\mu A$ for the cases of $\delta\rho = 15$Å and $\delta\rho = 30$Å (here, the effects of thermal broadening exceed those of the inhomogeneities so both $\delta\rho = 15$Å and $\delta\rho = 30$Å wires behave the same at room temperature). It is clear that the threshold current does not suffer much as the fabrication tolerance requirements are relaxed.

The modulation bandwidth is determined by the relaxation oscillation corner frequency,

$$f_c = \frac{1}{2\pi}\left[\frac{G'P_0}{\tau_p}\right]^{1/2} \tag{2.20}$$

where $G' = dG/dn$ is the differential gain , P_0 is the steady state photon density in the cavity, and τ_p is the photon lifetime [7]. Due to the sharpened density of states function, the differential gain for quantum wires should be higher than for bulk material. The differential gain can be found from Figs. 2.9 and 2.11. For the 50Å radius wires, the maximum differential gain is, dG/dn=1.0x10^{-15}cm^2 and 2.2x10^{-16}cm^2 for $\delta\rho = 2.5$Å and 10Å respectively. This is to be compared to a value of dG/dn=2.0x10^{-16}cm^2 for bulk GaAs, and dG/dn=5.0x10^{-16}cm^2 for quantum wells [8]. The differential gain for the 150Å wires, as calculated from Fig. 2.11, is close to the bulk value. We see that the modulation bandwidth of the well fabricated wire is greater by a factor of $\sqrt{5}$ than that of a laser with a bulk active layer, but that for more realistic fabrication tolerances the increased bandwidth disappears.

2.6 Conclusions

We have calculated the gain spectra of quantum wires accounting for fabricational inhomogeneities. The inhomogeneities were treated as a perturbation and it was found that to first order, the component of the perturbation that varies quickly compared to the coherence length of the carrier is averaged out and has no effect if the wire radius is chosen so that the roughness function has zero average. This indicates that the gain in quantum wires is somewhat insensitive to small scale inhomogeneities. An ensemble of wires with differing widths was considered and a bulk density of states and gain were calculated from this. According to these calculations, quantum wires with realistic fabrication tolerances are advantageous for low threshold laser applications but unless they are fabricated with atomic layer precision, they will not display a large enhancement in modulation bandwidth.

The wave functions for quantum wires have been examined using a finite cylindrical potential and we found a quasi-critical radius, below which, the carriers are not confined by the potential, although, in a strict sense, the state is a bound state. This puts a lower limit on the radius of quantum wires. An upper limit on the wire size is given by the requirement that the subbands be separated by an energy greater than k_BT and the effects of increasing the size and changing the number of quantized dimensions were tabulated for two-, one-, and zero-dimensional structure.

As a result of these calculations, it is concluded that quantum wire lasers with realistic fabrication tolerances are promising structures for reduced threshold current. Reductions of one to two orders of magnitude over the best quantum well lasers are possible. Such large reductions in threshold current could open new realms of applications for semiconductor lasers.

Bibliography

[1] K. Vahala, "Quantum Box Fabrication Tolerance and size Limits in Semiconductors and Their Effect on Optical Gain," *IEEE Journal of Quantum Electron.*, **QE-24**, 523 (1988).

[2] Abromawitz and Stegun, *Handbook of Mathematical Functions*, National Bureau of Standards, 1972.

[3] M. Asada, Y. Miyamoto, and Y. Suematsu, "Gain and the Threshold of Three-Dimensional Quantum-Box Lasers," *IEEE Journal of Quantum Electron.*, **QE-22**, 1915 (1986).

[4] M. Mittelstein, Y.Arakawa, A. Larsson, and A. Yariv, "Second Quantized State Lasing of a Current Pumped Single Quantum Well Laser," *Appl. Phys. Lett.*, **49**, 1689 (1986).

[5] P. L. Derry, A. Yariv, K. Y. Lau, N. Bar-Chaim, and J. Rosenberg, "Ultralow-Threshold Graded-Index separate-confinement Single Quantum Well Buried Heterostructure (Al,Ga)As Lasers With High Reflectivity Coatings," *Appl. Phys. Lett.*, **50**, 1773 (1987).

[6] H. C. Casey, Jr. and M. B. Panish, *Heterostructure Lasers* (Academic Press, New York, 1978).

[7] K. Y. Lau, N. Bar-Chaim, I. Ury, C. Harder, and A. Yariv, "11-GHz Direct Modulation Bandwidth GaAlAs Window Laser Operating at Room Temperature," *Appl. Phys. Lett.*, **45**, 316 (1984).

[8] Y. Arakawa, K.Vahala, and A.Yariv, "Dynamic and Spectral Properties of Semiconductor Lasers With Quantum-Well and Quantum-Wire Effects," *Surf. Sci.*, **174**, 155 (1986).

Chapter 3

Fabrication of Wire Structures by Impurity Induced Disordering

3.1 Introduction

Submicron bandgap tailoring of semiconductors has many applications such as optical waveguiding and carrier confinement. Growth techniques such as MBE allow for such tailoring in one dimension, but control of the other two dimensions of the material on this scale has been and remains a very challenging area of device research. Such lateral control permits fabrication of quantum wire and quantum dot structures. In Chapter 1, some of the techniques for fabricating quantum wires and dots, and some of the problems associated with these techniques were discussed. This chapter describes a set of experiments designed to use Zn diffusion to selectively disorder a quantum well and create quantum wires. This approach has the advantage that it creates neither free surfaces nor damage fields. The resulting structures are investigated in a scanning electron microscope (SEM) using cathodoluminescence (CL). Sections 3.2 and 3.3 provide brief introductions into the techniques of CL and disorder by impurity diffusion and Section 3.4 describes the fabrication and analysis of the wires.

3.2 Cathodoluminescence

Cathodoluminescence is the emission of light by a sample which is excited by an electron beam (cathode ray). Performing CL in an SEM allows one to take advantage of the existing electron optics and imaging capabilities. The sample can be viewed under high magnification by imaging of secondary electrons to locate specific regions of interest, and CL from these regions can be correlated with the surface features. The CL system employed here differs from most CL systems in that it allows for spectral analysis of the CL signal. With this system (which is described in detail elsewhere [1]) one end of an optic fiber is placed near the sample to collect the luminescence. The fiber passes out of the SEM by means of a high vacuum feedthrough and the light is then coupled into a monochromator (see Fig. 3.1). A cooled photomultiplier tube is placed on the output port of the monochromator. There are two basic modes of operation for this system. In one, the beam position is fixed while the monochromator scans through the wavelength region of interest. This generates a very local spectrum as in Fig. 3.4. Alternatively, the monochromator can be fixed at a specific wavelength while the electron beam is rastered across the sample, generating a spectrally resolved cathodoluminescence image (SRCI) as in Fig. 3.5. In this mode, the luminescence intensity at a given time is correlated with the beam position at that time to generate

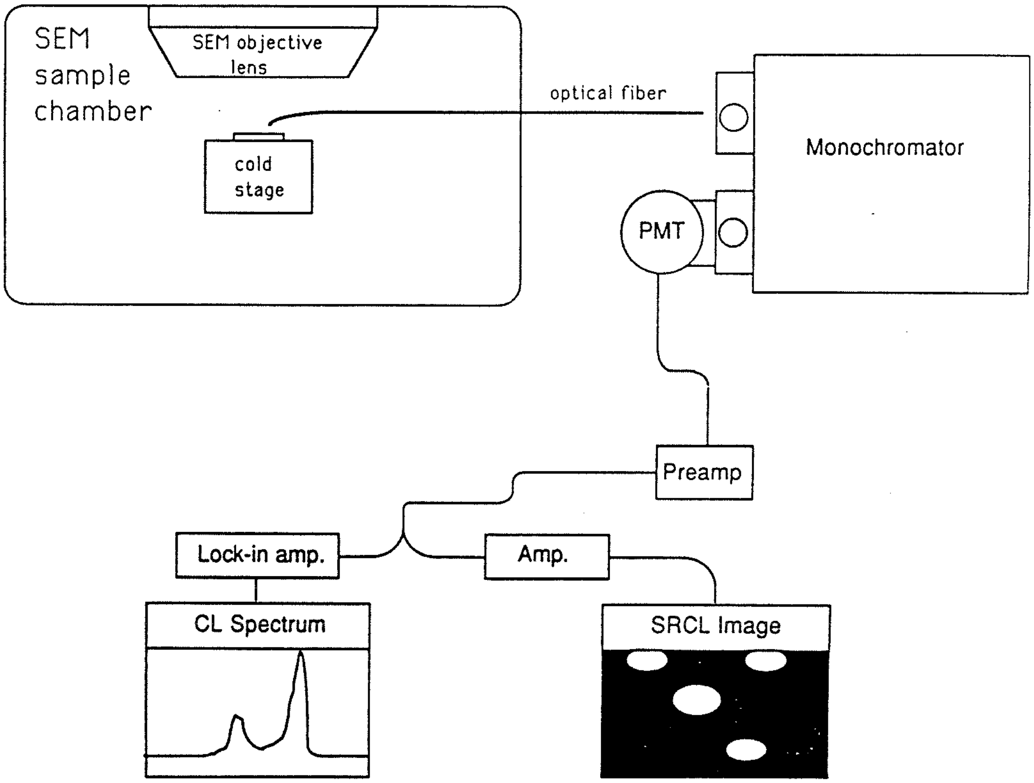

Figure 3.1: Diagram of the CL system.

the SRCI. For either mode, the spatial resolution is determined three parameters: the electron beam diameter, the volume in which carriers are generated (which depends on the penetration depth), and the carrier diffusion length. In a given situation, one of these factors will dominate and limit the resolution.

3.3 Disorder of GaAs/AlGaAs Structures by Impurity Diffusion

The success of the GaAs/AlGaAs material system relies, in part, on the stability of these heterostructures with regard to Ga-Al interdiffusion. Chang and Koma have shown that the activation energy for this process is quite high (≥ 3.6 eV) and the interdiffusion constant is small [2]. The essentially abrupt heterointerfaces remain sharp after thermal cycles as high as 925°C for several hours [3]. This permits processing at the elevated temperatures required for liquid phase epitaxy (LPE) regrowth ($\sim$ 800°C), the introduction of dopants by diffusion ($\sim$ 500°C — 800°C), the growth of SiO_2 ($\sim$ 320°C) and SiN_x ($\sim$ 720°C) films by chemical vapor deposition (CVD), and other steps in the fabrication of devices from these materials.

In contrast to this, it has been shown that the introduction of high concentrations of Zn causes appreciable Ga-Al interdiffusion at much lower temperatures (500°C — 600°C) [4]. This has been used to disorder AlGaAs/GaAs superlattices [4], and single quantum well structures [5], leaving a region of homogeneous $Al_xGa_{1-x}As$ with Al concentration, x, which is the average concentration for the superlattice or quantum well structure. By masking parts of the surface, Zn diffusion can be used to selectively disorder regions of the wafer, leaving other regions intact. This technique for locally altering the bandgap and index of refraction has been used in the fabrication of devices such as light emitting diodes (LED's) and semiconductor lasers, among others. Implantation of Si [6] ions as well as Si diffusion [7] have also proven to be effective for impurity induced disordering (IID).

The model for Zn diffusion assumes that Zn can exist in two forms in the GaAs crystal: as an interstitial, Zn_i^+, where it acts as a donor, and as a substitutional acceptor on a Ga site, Zn_{Ga}^- [8]. The diffusion process is dominated by the more mobile interstitial form, which proceeds through the crystal until it encounters a Ga vacancy where it makes a transition to the substitutional form. The transition between the two forms is described by the relationship

$$Zn_i^+ + V_{Ga} \rightleftharpoons Zn_{Ga}^- + 2h \tag{3.1}$$

where V_{Ga} and h represent a Ga vacancy and a hole respectively. Using the reaction of Eq. 3.1, and applying the law of mass action, it can be shown that the diffusion coefficient, D, is proportional to the square of the Zn concentration, C_{Zn} [8]. The C_{Zn}^2 dependence of D, which has been verified experimentally [9], is particularly significant in that it causes the Zn concentration to drop off abruptly, giving a very sharp front to the diffusion profile.

Although the process of Zn diffusion in GaAs is well understood, the mechanism for Zn IID is not. It was suggested by Laidig [4] that an intermediate stage occurs in Eq. 3.1, consisting of a complex of Zn and a group III vacancy, V_{III}

$$Zn_i^+ + V_{III} \rightleftharpoons (Zn_iV_{III})^+ \rightleftharpoons Zn_{III}^- + 2h. \tag{3.2}$$

The suggestion is that through the formation of the complex, the group III vacancy concentration is effectively increased, which increases the interdiffusion of the group III elements, Ga and Al. An alternative explanation given by Van Vechten explains the enhanced interdiffusion as resulting from an interaction of the interstitial Zn with defect complexes [11][1]. Regardless of the mechanism, the use of selective IID is a powerful technique for locally altering the composition and band structure of a GaAs/AlGaAs heterostructure.

3.4 Selective Disorder of a GaAs/AlGaAs Quantum Well by Zinc Diffusion

Here we report on a new approach to creating quantum confined structures using a shallow zinc diffusion technique to selectively disorder a GaAs quantum well. The technique is illustrated in Fig. 3.2. There is a quantum well 500Å below the surface, and a superlattice 2300Å below the quantum well. A Zn diffusion is performed that goes deep enough to disorder the quantum well, but not so deep as to disorder the superlattice. In this manner, the superlattice serves as a marking layer. A Si diffusion mask is deposited on the surface of the wafer. The lateral encroachment of Zn under the mask is approximately equal to the downward diffusion, leaving a narrow region of the quantum well under the center of the Si stripe which has not been disordered by the diffusion. This allows us to start with a mask whose width may be a few

---

[1] An excellent review article entitled "Mechanisms of atomic diffusion in the III-V semiconductors" has been written by Brian Tuck [10].

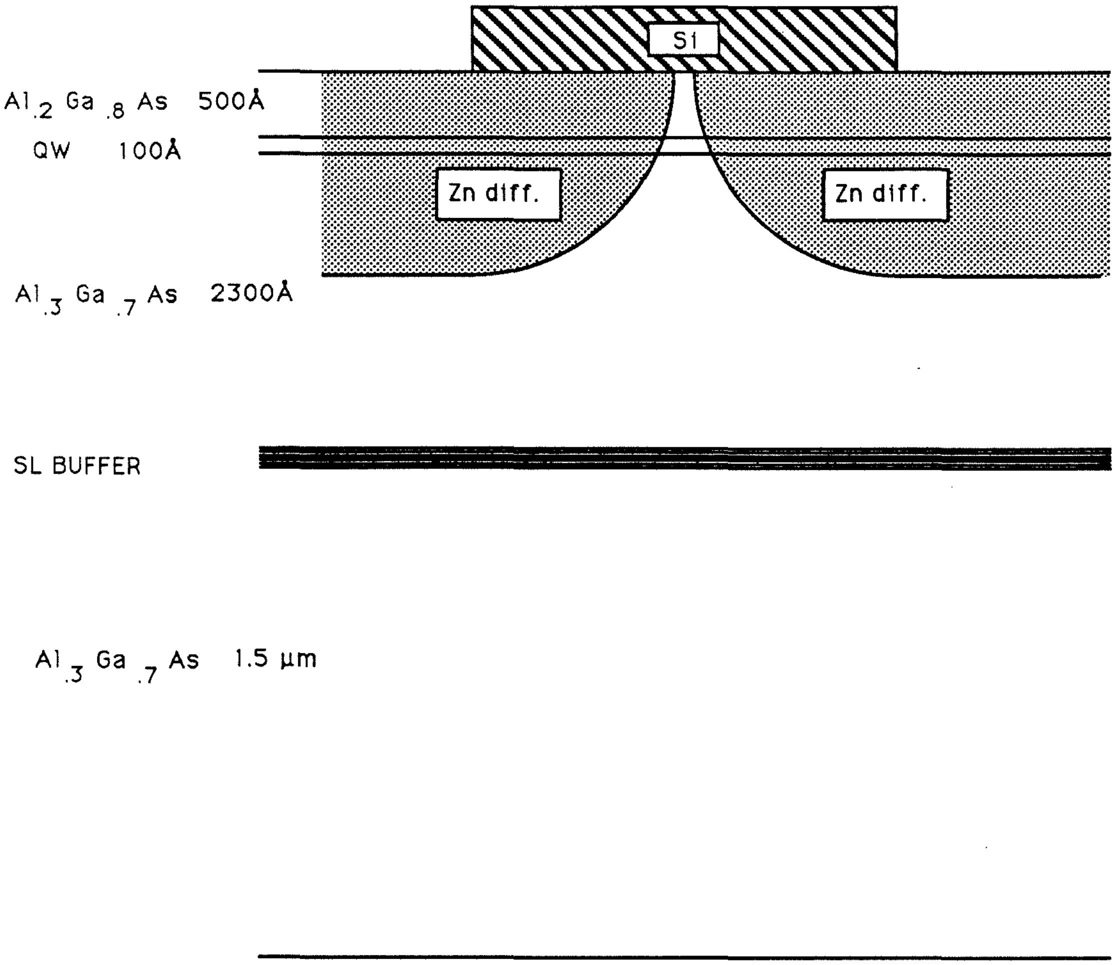

Figure 3.2: Schematic cross section of the wafer after Zn diffusion.

thousand angstroms and create a confining region that may be only a few hundred angstroms wide. By placing several stripe masks of different widths on the same sample, we increase the chance of achieving the correct diffusion depth.

It is well known that certain mask materials enhance lateral diffusion sometimes showing as much as 20 times that of vertical diffusion. This has been correlated with stress at the mask-wafer interface [12]. Because we were attempting to create a submicron structure using diffusion, it was imperative that the degree of lateral diffusion be small and reproducible. Silicon has been shown to be an excellent mask material for zinc diffusion [13]. Our experiments with SiN_x and Si showed that both materials work well, but SiN_x, if it has some SiO_2 in it, enhances the lateral diffusion. Because the Si mask is made by evaporating elemental Si in an ultra-high vacuum (10^{-7} torr) chamber, it proved to be more reproducible. Measurements were performed to investigate the degree of lateral diffusion under a silicon mask. For these studies, diffusions over much longer periods of time were performed to achieve much deeper diffusion fronts. After diffusion, CL measurements confirmed that the quantum well was intact under the masked areas and completely disordered in unmasked areas. The disordering was observed to extend approximately one micron under the mask, indicating the presence of lateral diffusion. Sample cross sectioning and staining, followed by examination in an optical microscope confirmed this observation. The diffusion front was seen to have moved laterally under the mask a distance roughly equal to that in the downward direction.

The sample was grown by molecular beam epitaxy in a Riber 2300 R & D system.

The layers were grown in the following order: a 1μm GaAs buffer layer, a 500Å AlAs blocking layer, a 1.5μm $Al_{0.3}Ga_{0.7}As$ buffer layer, a superlattice buffer layer consisting of three 70Å GaAs layers separated by 70Å $Al_{0.3}Ga_{0.7}As$ layers, a 0.23μm $Al_{0.3}Ga_{0.7}As$ layer, a 100Å GaAs quantum well, and a 500Å $Al_{0.17}Ga_{0.83}As$ cap layer. All layers were undoped.

The diffusion mask was created on this sample using a combination of electron beam lithography and a silicon lift off technique. The sample was spin coated with a 3 percent polymethylmethacrylate (PMMA) solution at 3500 rpm. Electron beam lithography was performed in a modified Cambridge Instruments S-240 scanning electron microscope (SEM). Narrow lines, 4.5μm long, ranging from 1600Å to 5000Å in width, were written in array patterns and as isolated lines. In addition, regions 40 μm square were exposed uniformly to provide a broad mask for comparison. After development, the sample was placed in an electron beam evaporator and a 500Å layer of silicon was deposited. Lift off was done with dichloromethane. Fig. 3.3 shows a typical array of silicon stripes on the surface of the sample.

Following the standard procedure for zinc diffusion in GaAs, the sample was sealed in an evacuated, fused quartz ampoule with solid zinc arsenide as the diffusion source. A series of diffusion calibrations established that a one hour diffusion at 535 °C was sufficient to disorder the quantum well, but not so deep as to disorder the superlattice. This placed the disorder front at a depth between 600Å and 2800Å. For these calibration measurements the CL system was used to measure the disappearance of the quantum well emission peak as well as the spatial uniformity of the diffusion pro-

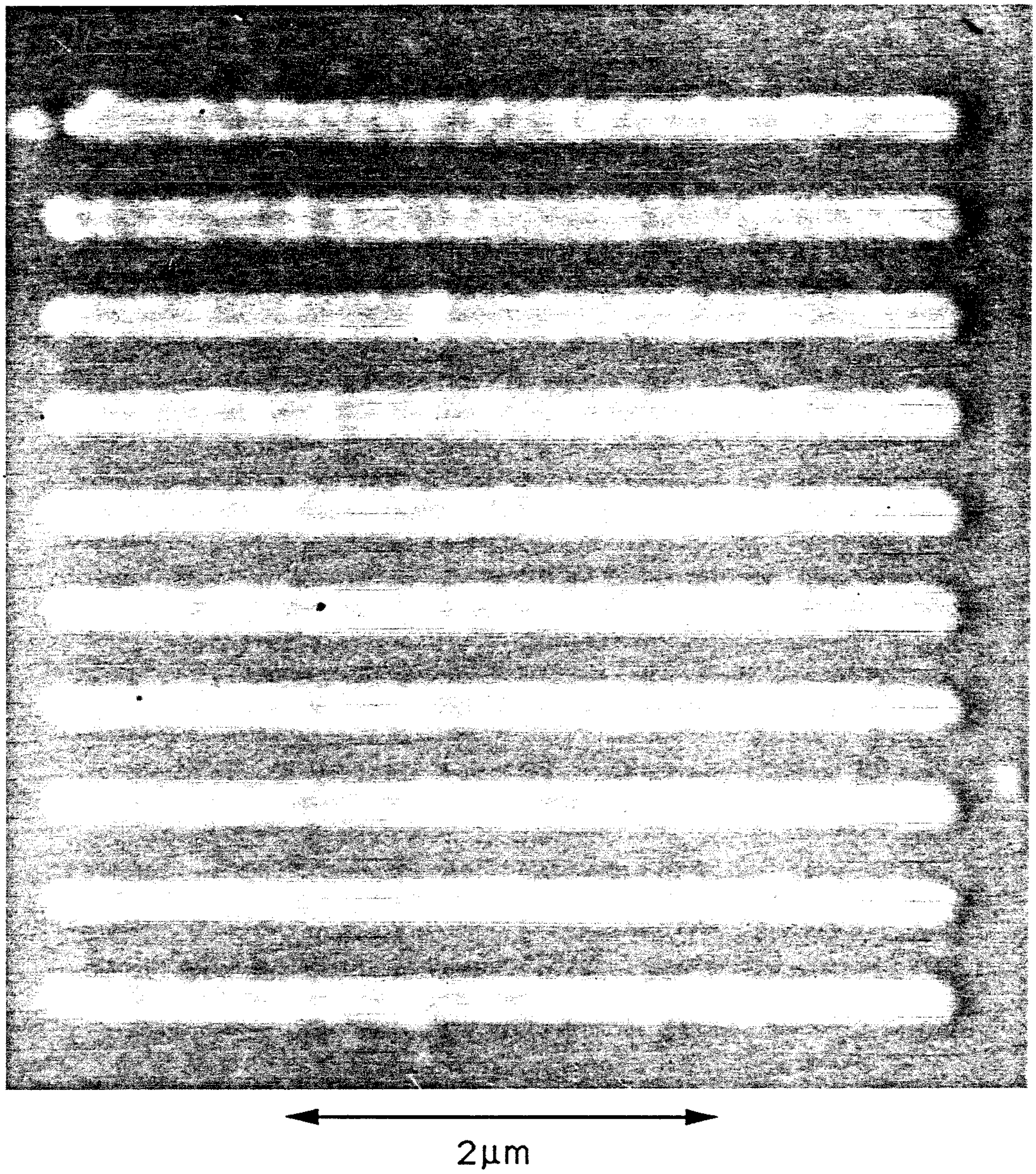

Figure 3.3: Scanning electron micrograph of a typical diffusion mask array of silicon stripes.

cess. CL spectra from uniformly masked and unmasked areas of the sample (after the 535 °C diffusion) are presented in Fig. 3.4. The spectra were taken under excitation by 20kV electrons at a current of approximately 200nA at a temperature of 77 K. Two peaks appear in the spectrum from the uniformly masked region. The smaller peak at 789nm is identified as the quantum well and the peak at 772nm is the superlattice. The relative intensities of these peaks are controlled by the accelerating voltage of the excitation beam and is not an indication of the relative quality of the layers. By using a lower acceleration voltage we obtained spectra where the quantum well peak is much stronger than the superlattice. The spectrum from the uniformly masked region was found to be identical in form to a sample spectrum taken prior to the diffusion. This shows that the broad area mask successfully protected the quantum well during the diffusion and that all changes noted below can be attributed to the diffusion process (i.e., not to other effects such as temperature cycling).

On the same sample were a series of silicon wire masks. Fig. 3.5 shows both the secondary electron and CL images of a region containing seven arrays of wires and several single wires. The left half of the figure shows the conventional SEM micrograph of the silicon wires. The elements of the arrays range from 1600Å wide (lower right array) to 3700Å wide (upper left array). The single lower wire is 5000Å wide. The right half of the figure shows the same structures except now viewed using spectrally resolved CL with the wavelength adjusted to 780 nm. The wavelength of 780 nm was found to give the greatest contrast between the wires and the background. This wavelength is intermediate to the peak emission wavelength of the quantum well

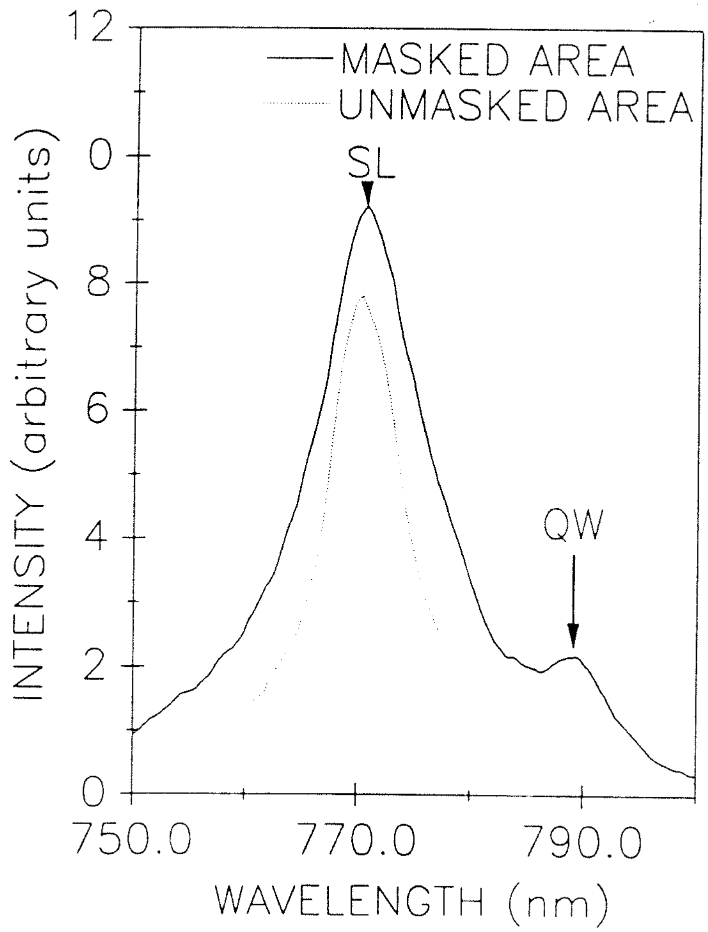

Figure 3.4: Cathodoluminescence spectra of a uniformly masked region and an unmasked region. The sample temperature is 77 K.

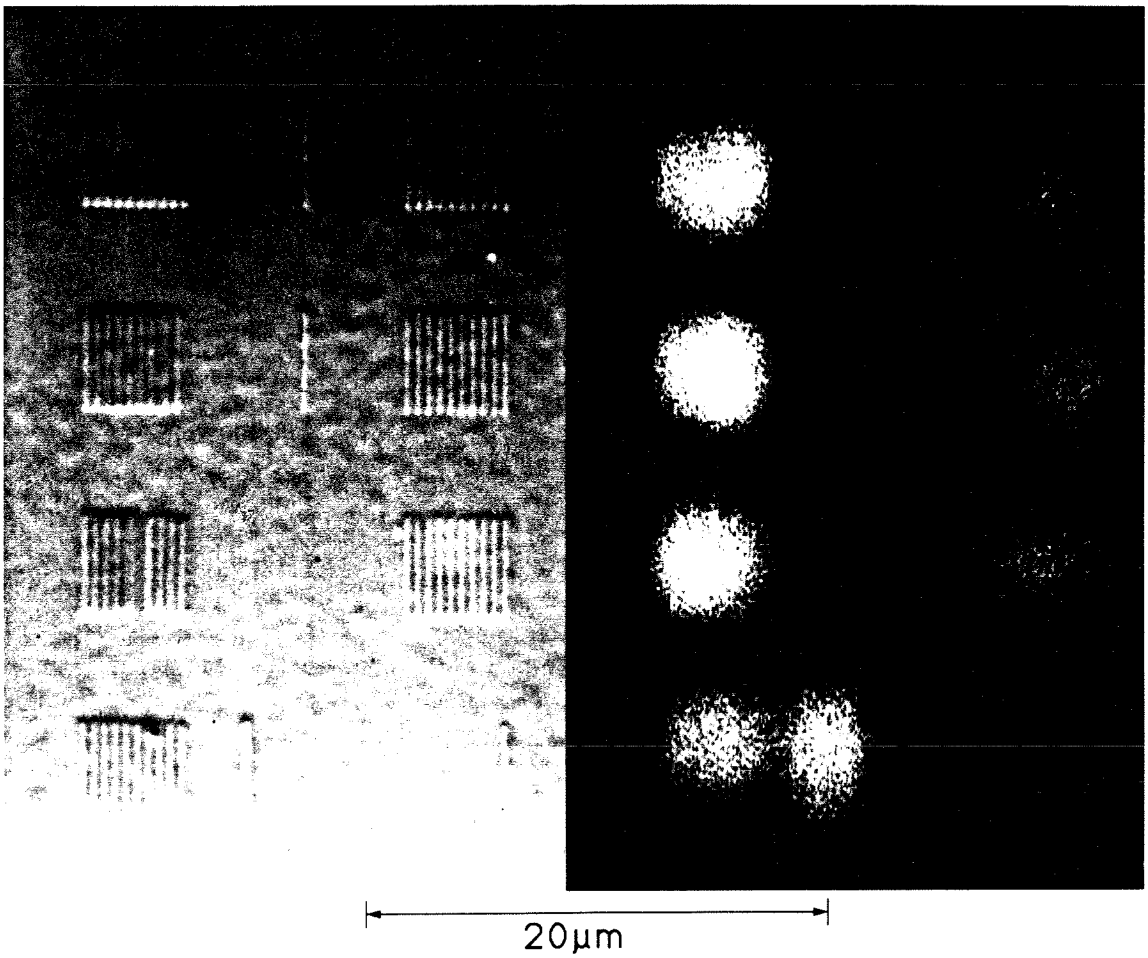

Figure 3.5: Secondary electron and cathodoluminescence images of several arrays of wires and an isolated wire. The left half shows the silicon mask as a conventional SEM micrograph. The width of the silicon stripes in the arrays varies from 3700Å (upper left array) to 1600Å (lower right array). The right half shows the spectrally resolved cathodoluminescence image of the same region at a wavelength of 780 nm. The sample temperature is 77 K.

and the superlattice, which suggests that the diffusion has altered the luminescence spectra of the regions under the wire masks. Due to carrier diffusion, CL is not able to resolve the individual elements in each array, but the single 5000Å element is resolved. All arrays tested generated CL images similar to those shown in Fig. 3.5.

Cathodoluminescence spectra of individual arrays were taken by placing the electron beam at the center of an array. Spectra of arrays with mask stripe widths of 3700Å (broad wires) and 3100Å (narrow wires) are shown in Fig. 3.6. The spectra were taken under excitation by 10kV electrons at a current of approximately 20nA at a temperature of 12K. The emission spectra from the broad and narrow wire array structures are intermediate to both the superlattice peak and the quantum well peak. (The quantum well and superlattice peak positions shown in Fig. 3.6 are as measured at 12K, not at 77K as in Fig. 3.4). Because the superlattice emission peak is unshifted by the diffusion, we conclude that the quantum well peak is blue shifting to produce the peaks seen in the wire spectra. Shifts of 21 meV and 30 meV are seen in the broad and narrow wire arrays as compared to the quantum well. Spectra from masked areas containing narrower stripes exhibited features that were merging with those of the background spectra. One mechanism for the observed blue shift on the array spectra is increasing confinement by the lateral diffusion induced potential. The observed shifts are appropriate for a square potential of $\approx$ 150Å. It is expected that the width of the confinement potential would decrease with decreasing mask width, and furthermore, that the actual potential width will be narrower than the mask width due to lateral zinc diffusion. Although the blue shift increases with decreasing

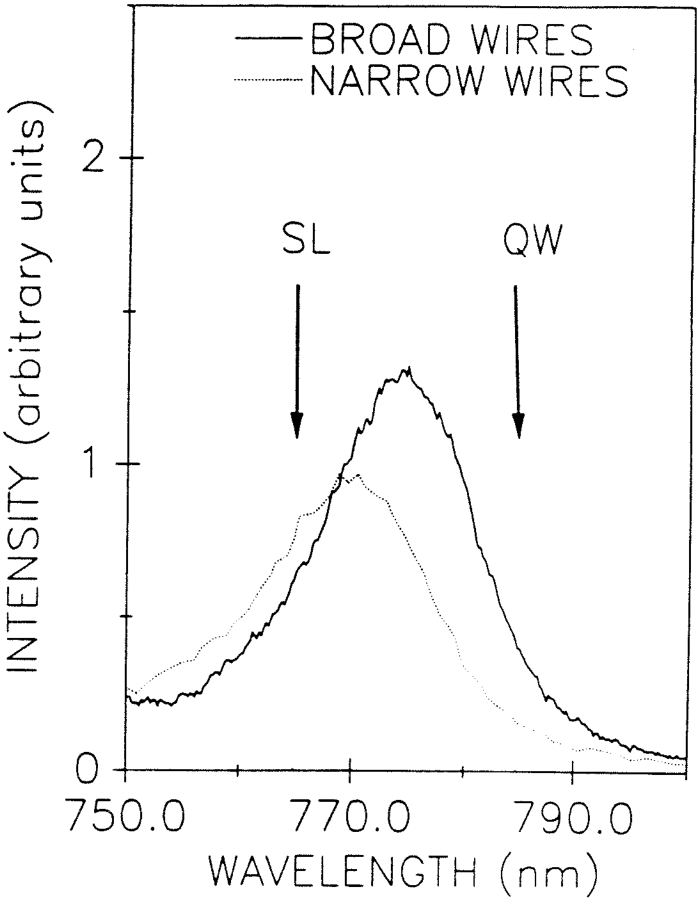

Figure 3.6: Cathodoluminescence spectra of a 3700Å wide wire masked region, and a 3100Å wide wire masked region. The sample temperature is 12K. The peak positions of the quantum well and superlattice at this temperature are indicated by the arrows.

mask width, the change in the luminescence peak energy as the mask width changes does not correlate well with the expectations for a square potential. Rough fits to a more gradual potential can be made but this is of questionable value without a good knowledge of the form of the actual potential. For this reason, it is not possible to attribute this to a quantum size effect with certainty. Another possible mechanism for producing the observed shifts is the introduction of a small amount, approximately 2 percent, of aluminum into the quantum well. The observed shifts may, in fact, be due to a combination of these two mechanisms.

In conclusion, we have employed a zinc diffusion technique to create a lateral bandgap variation in a GaAs quantum well. The diffusion process utilized a mask of silicon stripes as narrow as 1600Å to induce selective disordering of the quantum well. Spectrally resolved cathodoluminescence micrographs were presented showing selectively disordered patches of wire structures. Local cathodoluminescence spectra indicate that the emission spectra from the wire structures is blue shifted. Regardless of the origin of these shifts, it is clear that this technique has produced lateral bandgap modulations on a nanometer scale.

Bibliography

[1] M. E. Hoenk and K. J. Vahala, "Cathodoluminescence system for a scanning electron microscope using an optic fiber for light collection, *Rev. Sci. Instrum.*, **60**, 226 (1989).

[2] L. L. Chang and A. Koma, "Interdiffusion between GaAs and AlAs," *Appl. Phys. Letts.*, **29**, 138 (1976).

[3] W. D. Laidig, N. Holonyak, Jr., M. D. Camras, B. A. Vojak, K. Hess, J. J. Coleman, and P. D. Dapkus, "Quenching of Stimulated Emission in $Al_xGa_{1-x}As$ Quantum-Well Heterostructures," *Solid State Commun.*, **38**, 301 (1981).

[4] W. D. Laidig, N Holonyak, Jr., M. D. Camras, K. Hess, J. J. Coleman, P. D. Dapkus, and J. Bardeen, "Disorder of an AlAs-GaAs superlattice by impurity diffusion,"*Appl. Phys. Letts.* **38**, 776 (1981).

[5] K. Meehan, J. M. Brown, M. D. Camras, N. Holonyak, R. D. Burnham, T. L. Paoli, and W. Streifer, "Impurity-induced disordering of single well $Al_xGa_{1-x}As$ quantum well heterostructures," *Appl. Phys. Letts.*, **44**, 428 (1984).

[6] J. J. Coleman, P. D. Dapkus, C. G. Kirkpatrick, M. D. Camras, and N. Holonyak,

Jr., "Disorder of an AlAs-GaAs superlattice by silicon implantation," *Appl. Phys. Letts.*, **40**, 904 (1982).

[7] K. Meehan, N. Holonyak, Jr., J. M. Brown, M. A. Nixon, P. Gavrilovic, and R. D. Burnham, "Disorder of an $Al_xGa_{1-x}As$-GaAs superlattice by donar diffusion," *Appl. Phys. Letts.*, **45**, 549 (1984).

[8] R. L. Longini, "Rapid Zinc Diffusion in Gallium Arsenide," *Solid State Electron.*, **5**, 127 (1962).

[9] M. A. Kadhim and B. Tuck, "Isoconcentration Diffusion of Zinc in GaAs at 1000°C," *J. Matter. Sci.*, **7**, 68 (1972).

[10] B. Tuck, "Mechanisms of atomic diffusion in the III-V semiconductors," *J. Phys. D: Appl. Phys.*, **18**, 557 (1985).

[11] J. A. Van Vechten, "Intermixing of an AlAs-GaAs superlattice by Zn diffusion," *J. Appl. Phys.*, **53**, 7082 (1982).

[12] B. J. Baliga and S. K. Ghandi, "Lateral Diffusion of Zinc and Tin in Gallium Arsenide," *IEEE Trans. on Electron Devices*, **ED-21**, 410 (1974).

[13] E. Omura, G. A. Vawter, L. Coldren, and J. L. Merz, "Selective Zn diffusion mask in *n*-GaAs with a sputtered Si mask at 650°C,"*Electron. Letts.*, **22**, 23 (1986).

Chapter 4

Direct Determination of the Carrier Diffusion Length in GaAs/AlGaAs Heterostructures by Cathodoluminescence

4.1 Introduction

Transport properties of GaAs/AlGaAs heterostructures are of great interest due to the importance of these structures for optoelectronic devices, high electron mobility transistors (HEMT), resonant tunneling diodes, etc. Carrier diffusion lengths (minority and ambipolar) are important both as transport parameters and as quantities that can be used to obtain information on carrier lifetime or mobility. Many methods have been used to measure diffusion lengths, most notably, the Haynes-Shockley experiment [1]. More recently, techniques such as short-circuit photocurrent measurements [2], electron beam induced currents [3], transient grating techniques [4], and time of flight studies [5] have been applied. Here, we present a new technique for determining the carrier diffusion length using cathodoluminescence (CL). This method can be applied to direct gap semiconductors to determine either minority carrier or ambipolar diffusion depending on the sample doping and excitation conditions. Due to the precision and ease with which one can control the position of the electron beam in a scanning electron microscope (SEM) the method is very straightforward and accurate. Furthermore, the ability to examine the sample under the high magnifications available with an SEM allows this technique to be applied to submicron devices and microstructures such as quantum wires. In this chapter we apply the technique to ambipolar diffusion in undoped samples of GaAs quantum well material, bulk GaAs, $Al_{0.19}Ga_{0.81}As$, and $Al_{0.35}Ga_{0.65}As$.

4.2 Description of the Technique

The experiment is performed in a modified SEM with the fiber optic CL collection system described in Section 3.2. In the SEM, an energetic electron beam is incident upon the sample, generating electron-hole pairs within the interaction region of the beam with the sample. One end of the fiber is placed approximately 0.5mm from the sample, collecting luminescence from a region approximately $100\mu m$ in radius while the other end is coupled into a monochromator allowing spectral resolution of the CL signal. The luminescence is chopped and detected with a cooled photomultiplier tube and lock-in amplifier. A thin aluminum mask covers half of the sample and prevents detection of the luminescence emanating from the region under it. All detected luminescence is from radiative recombination that occurred in the unmasked region. This is shown schematically in Fig. 4.1. By generating the carriers in the masked region of the sample and measuring the luminescence intensity as a function of the distance of the beam from the mask edge, $I(x)$, we are able to determine the diffusion length, L_D. To allow different material compositions to be investigated on a single sample, carriers were confined to narrow channels of the material being studied by high bandgap barriers on either side. It is important that the barriers be thin compared to x so that only those carriers that were generated in the channel contribute to its CL signal. Samples typically contained two channels of different material composition, and signals from different channels were separated with the monochromator.

The simplicity of the technique results from the fact that the luminescence signal depends exponentially on x/L_D.The exponential dependence on x is significant not only because of the ease with which it is handled numerically, but also because it allows us to ignore the size and shape of the interaction region so long as it remains completely under the aluminum mask.

4.3 Argument for Exponentially Decaying Signal

In this section we show that luminescence signal decays exponentially with the distance of the beam from the mask edge, and that the characteristic length of the

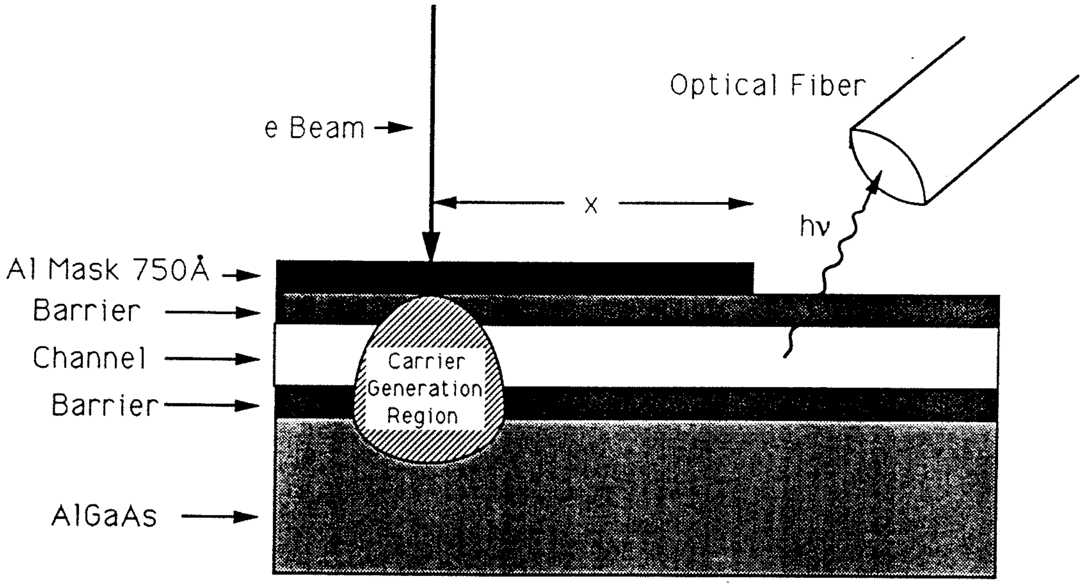

Figure 4.1: Schematic diagram of the experiment. An electron beam is incident on the sample, generating electron hole pairs. Luminescence is collected with the optical fiber. The Al mask blocks detection of luminescence from the region under it.

exponential is the diffusion length. We present two arguments demonstrating this. The first is a numerical calculation based on a cylindrically symmetric charge distribution, and the second is based on the principle of superposition. Finally, we extend the argument to an arbitrary charge distribution.

Because the fiber collects light from a region that is of much larger dimension than the carrier diffusion length, we may assume that all carriers that diffuse into the unmasked region contribute to the luminescence signal. The luminescence signal is then proportional to the net flux of carriers into the unmasked region.

The carrier concentration is governed by the continuity equation

$$\frac{\partial C}{\partial t} = G - R - \frac{1}{q}\vec{\nabla} \cdot \vec{J} \tag{4.1}$$

where $C, \vec{J}, G, R$ are the carrier concentration, current, generation rate, and recombination rate for the minority carriers and q is the carrier charge (negative for electrons). For the zero field case, the current is purely diffusive and is determined by Fick's law

$$\vec{J} = -qD\vec{\nabla}C \tag{4.2}$$

where D is the diffusion coefficient. The electron beam generates carriers in a volume with finite radius ρ_G. Outside of this volume, $G = 0$. Furthermore, if we assume steady state conditions, and recombination of the form $R = C/\tau$, Eqs. 4.1 and 4.2 combine to give

$$0 = -\frac{C}{\tau} + D\nabla^2 C, \qquad \text{for } \rho > \rho_G, \tag{4.3}$$

where τ is the carrier lifetime. The barriers in the samples prevent diffusion perpendicular to the channel, eliminating one dimension from the problem. For the two-dimensional case with circular symmetry, Eq. 4.3 is Bessel's equation of zeroeth order and the only solution that fits the boundary condition at $\rho = \infty$ is the modified Bessel function of zeroeth order

$$C(\rho) = C_0 K_0 \left(\frac{\rho}{L_D}\right), \qquad \text{for } \rho > \rho_G, \tag{4.4}$$

where

$$L_D \equiv \sqrt{D\tau} \tag{4.5}$$

is the diffusion length, C_0 is a constant and ρ_G is the radius of the generation volume. This solution can be used to calculate the flux of carriers into the unmasked region as a function of the distance of the generation volume from the mask edge, x. This is given by

$$F(x) = \int_{-\infty}^{\infty} \vec{\nabla} C \cdot \vec{dl} \tag{4.6}$$

where the integral is performed along the mask edge (see Fig. 4.2). In rectangular coordinates, $\vec{dl} = dy\vec{e_x}$, where $\vec{e_x}$ is the unit vector in the x direction. Inserting Eq. 4.4 into Eq. 4.6 and using the relation $dK_0(z)/dz = -K_1(z)$ [6] gives

$$F(x) = \frac{C_0}{L_D} \int_{-\infty}^{\infty} \frac{x}{\sqrt{x^2 + y^2}} K_1(x^2 + y^2) dy. \tag{4.7}$$

We were not able to solve the integral of Eq. 4.7 analytically, but evaluating it numerically gives a result which, to several significant figures and over a range spanning several orders of magnitude, is indistinguishable from $F(x) \propto e^{-x/L_D}$. The simplicity of this result as compared with the complex appearance of Eq. 4.7 led us to search for the following, "physical" explanation.

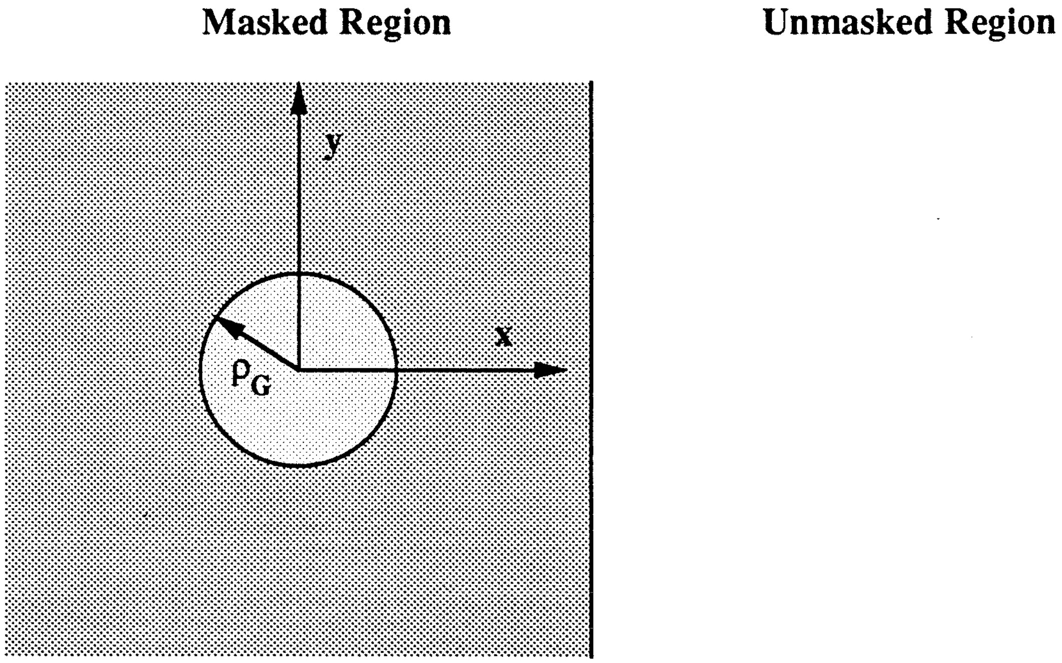

Figure 4.2: Coordinates for the flux calculations. A cylindrically symmetrical charge generation region of radius ρ_G is shown. The integral of Eq. 4.7 is performed along the boundary between the masked and unmasked regions.

First, let us examine diffusion in one dimension. In this case, the solution to Eq. 4.3 is $C = C_0 e^{-x/L_D}$, which yields

$$F_{1D} = -\frac{C_0}{L_D} e^{-x/L_D} \tag{4.8}$$

where F_{1D} represents the flux into the unmasked region due to a point charge in the one-dimensional case. Next, assume that we generate a line of constant carrier density, parallel to, and a distance x from the mask edge (see Fig. 4.3). By symmetry we know that this is equivalent to the one-dimensional problem. We define $R_n(x, y - y_n)$ as the response due to the n^{th} element of the line, that is, $R_n(x, y - y_n) = \vec{\nabla} C_n \cdot \vec{dl}$. Equation 4.6 can be written as

$$F_l(x) = \int_{-\infty}^{\infty} dy \sum_{n=0}^{\infty} R_n(x, y - y_n) \tag{4.9}$$

where $F_l(x)$ is the flux due to a line of charge. Because the line stretches to infinity, we need not keep track of the position of the element along the line and Eq. 4.9 becomes

$$\begin{aligned} F_l(x) &= \int_{-\infty}^{\infty} dy \sum_{n=0}^{\infty} R_n(x, y) && (4.10) \\ &= N \int_{-\infty}^{\infty} dy R_n(x, y) && (4.11) \end{aligned}$$

If the elements of the line are small enough, $R_n(x, y)$ represents the response due to a point charge, so by equating Eqs. 4.8 and 4.11 we conclude that for a point source,

$$F(x) \propto e^{-x/L_D}. \tag{4.12}$$

While there may be certain cases where the carrier generation region may be well approximated by a point source, to be useful in a more general way, the argument

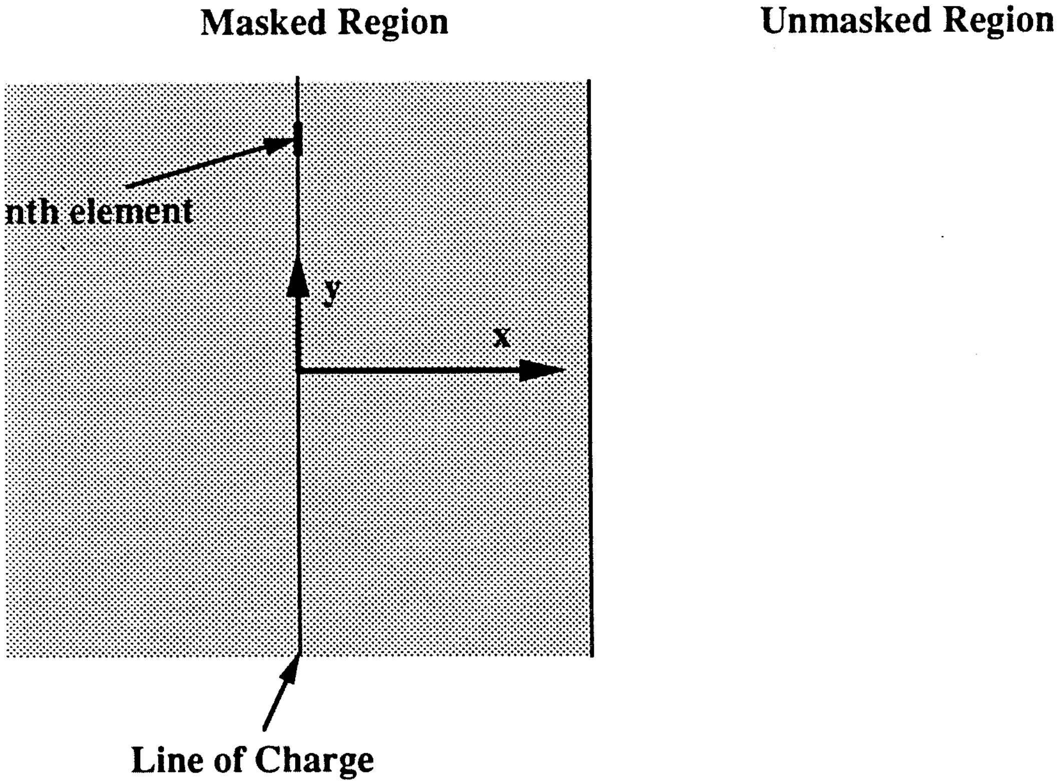

Figure 4.3: Coordinates for the flux calculations for a lineal charge distribution.

must be extended to a more realistic generation volume. We now show that Eq. 4.12 applies for a generation region of arbitrary size and shape with the only restriction being that it must lie entirely underneath the mask.

Figure 4.4 diagrams an arbitrarily shaped interaction volume. The flux due to a small element in the generation volume is given by

$$F_i(x) = A_i e^{-x_i/L_D}, \tag{4.13}$$

and the net flux is given by

$$F(x) = \sum_i F_i = \sum_i A_i e^{-x_i/L_D}. \tag{4.14}$$

Equation 4.13 can be rewritten as

$$F_i(x) = A_i e^{-x_i'/L_D} e^{-x/L_D} \equiv A_i' e^{-x/L_D}, \tag{4.15}$$

where x is the smallest distance from the mask edge to the generation volume, and x_i' is a constant. Putting Eq. 4.15 into Eq. 4.14 gives

$$F(x) = \sum_i A_i' e^{-x/L_D} = e^{-x/L_D} \sum_i A_i'. \tag{4.16}$$

Therefore, the net flux of carriers into the unmasked region is of the form $F(x) = Ae^{-x/L_D}$ regardless of the shape and size of the generation volume, so long as x is positive. It is worth noting that although the argument presented here was for diffusion in two dimensions, it can easily be extended to the three-dimensional case. This would be useful if the technique were applied to bulk materials, which do not have barriers confining the carriers to a channel.

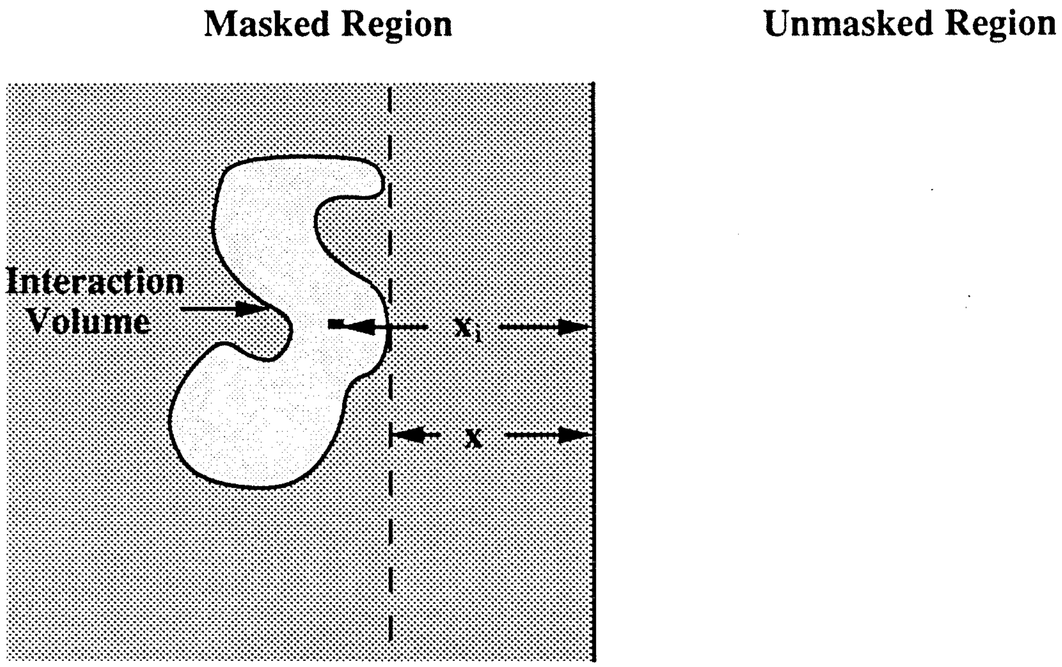

Figure 4.4: An arbitrary shape charge generation volume.

4.4 Experimental Conditions and Results

The samples used in the experiment were grown by molecular beam epitaxy (MBE) in a Riber 2300 R & D system. Sample 1 had a 750$\AA$ $Al_{0.35}Ga_{0.65}As$ channel and a 750$\AA$ GaAs channel both with AlAs barriers while Sample 2 had a 750$\AA$ $Al_{0.19}Ga_{0.81}As$ channel with AlAs barriers and a 100$\AA$ GaAs quantum well channel with $Al_{.3}Ga_{.7}As$ barriers. The determination of the Al mole fraction was accomplished by room temperature photoluminescence (PL) measurements. The PL spectra were taken using a relatively low intensity ($\approx$ 1W/cm^2) excitation by the 5145Å line of an Argon ion laser, and Al mole fractions, x, were determined from the PL spectra peak energy, E_p, using the relation $E_p(eV) = 1.42 + 1.45x - 0.25x^2$, which has been shown to hold for $0 < x \leq 0.45$ and similar excitation conditions [7]. There was no intentional doping in either sample. Stripes of aluminum, 750$\AA$ thick and 100μm wide were evaporated onto the surface. While thin enough to allow the electron beam to penetrate into the sample, this mask was found to be sufficiently thick to prevent detection of a luminescence signal through it. The sample was excited by a 10kV electron beam with a current of approximately 20nA. This yields a carrier density on the order of 10^{18}cm^{-3} in the generation volume. With a 10 kV beam, the generation volume has a radius of approximately 0.1μm in the channels [8]. For the GaAs, quantum well, and $Al_{0.35}Ga_{0.65}As$ channels, the beam position was varied from 3.33μm to 0.91μm from the mask edge in steps of 485$\AA$ with a dwell time of 0.5 seconds. Due to the shorter diffusion length in the $Al_{0.19}Ga_{0.81}As$ channel, the range of x was shortened to run between 2.12μm and 0.93μm in steps of 250$\AA$. Figure 4.5 shows typical data runs for three different channels. The data is quite linear and there is very little scatter. All data presented here were taken at room temperature. When the sample was cooled to liquid nitrogen temperatures, it was observed that the exposure to the electron beam altered the luminescence strength and diffusion length of the material. Similar electron beam effects [9] and laser excitation effects [10] have been observed by others. Material in the region of the mask was most severely affected, leading us to suspect that it is strain related. This effect was observed to a lesser degree at room temperature so care was taken to take data on previously unexposed regions of the sample. While taking data, the beam was scanned toward the mask edge to assure that material between the beam and the mask edge had not been altered by the beam. Once these precautions were taken, the data was found to be quite reproducible and consistent across the sample.

Table 4.1 summarizes the data for each channel. The diffusion lengths given represent an average over four measurements in different regions of the sample. The extremely small standard deviations demonstrate the precision of the technique. For the quantum well material, L_D is approximately the same as in the GaAs channel. The reduction in the diffusion length for the $Al_{0.19}Ga_{0.81}As$ channel can be attributed to a reduced mobility due to alloy scattering and increased effective mass [11]. A surprising result is the extremely large diffusion length for the $Al_{0.35}Ga_{0.65}As$ material. Increased alloy scattering, intervalley scattering, and effective mass, cause further reductions in the mobility, leading us to conclude that it is an increased lifetime that is responsible for the large L_D. The aluminum mole fraction of 0.35 is close to the transition

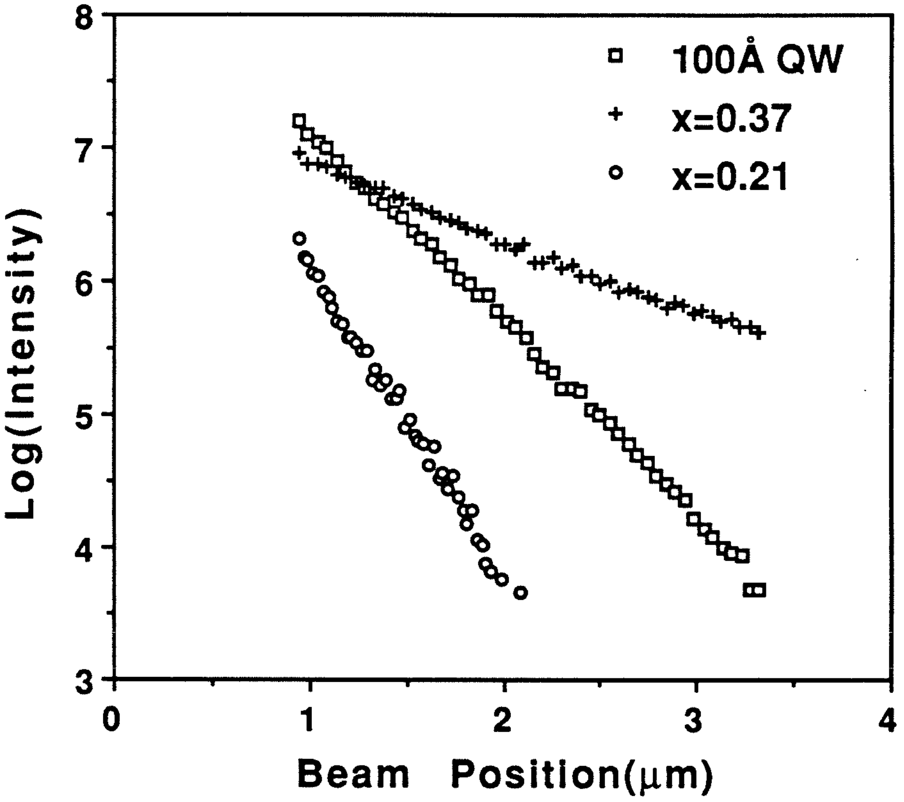

Figure 4.5: Log of the cathodoluminescence intensity as a function of beam position for quantum well, $Al_{.35}Ga_{.65}As$, and$Al_{0.19}Ga_{0.81}As$ channel. The ambipolar diffusion length is given by the reciprocal of the slope.

Material	GaAs	Q. W	$Al_{0.19}Ga_{0.81}As$	$Al_{0.35}Ga_{0.65}As$
$\overline{L_D}(\mu m)$	0.69	0.68	0.48	1.85
$\sigma(\mu m)$	0.01	0.02	0.02	0.1

Table 4.1: Ambipolar diffusion length, L_D, in the 4 materials studied. The value of L_D given is an average of 4 measurements taken in different regions of the sample and σ is the variance.

point where $Al_xGa_{1-x}As$ becomes an indirect gap semiconductor. At this point, both the X and L valleys are approximately $2k_BT$ above the Γ valley making them all thermally accessible to the carriers at room temperature[12,13]. The lifetime in these indirect valleys can be quite long and the density of states there is large. Because intervalley scattering times are short compared to carrier lifetimes, the carriers will scatter between the valleys and may spend a substantial fraction of the time in the indirect valleys before recombining. Using the electron mobility data of Ref. [11], and a heavy hole mobility calculated from Ref. [14], our L_D measurements imply an 8.5 times increase in lifetime. This is in the 25ns range. The dependence of the diffusion length and the carrier lifetime on the Al mole fraction is examined in more detail in Chapter 5.

4.5 Conclusions

In conclusion, we have presented a new method for measuring either minority carrier or ambipolar diffusion lengths by cathodoluminescence. The technique is extremely accurate due to the precision with which one can position an electron beam in a SEM. A simple exponential dependence of the CL intensity with beam position facilitates extraction of L_D from the data. An unexpectedly large L_D was measured for $Al_{0.35}Ga_{0.65}As$ and, with knowledge of the mobility, L_D was used to infer a lifetime.

Bibliography

[1] J. R. Haynes and W. Shockley,"The Mobility and Life of Injected Holes and Electrons in Germanium," *Phys. Rev.*, **81**, 835 (1951).

[2] H. C. Casey Jr., B. I. Miller, and E. Pinkas, "Variation of minority-carrier diffusion length with carrier concentration in GaAs liquid-phase epitaxial layers," *J. Appl. Phys.*,**44**, 1281 (1973).

[3] C. van Opdorp, R. C. Peters, and M. Klerk,"Use of Schottkey-diode collectors for SEM determination of bulk diffusion lengths," *Appl. Phys. Letts.*, **24**, 125 (1974).

[4] K. Hattori, T. Mori, H. Okamoto, and Y. Hamakawa, "Carrier transport property in the amorphous silicon/amorphous silicon carbide multilayer studied by the transient grating technique,"*Appl. Phys. Letts.*, **51**, 1259 (1987).

[5] H. Hillmer, S. Hansmann, A. Forchel, E. Lopez, H. P. Meier, and K. Ploog, "Two-dimensional exciton transport in GaAs/AlGaAs quantum wells," *Appl. Phys. Letts.*, **53**, 1937 (1988).

[6] Abromawitz and Stegun, *Handbook of Mathematical Functions*, National Bureau of Standards, 1972.

[7] N. C. Miller, S. Zemon, G. P. Werber, and W. Powaazinik, "Accurate electron probe determination of aluminum composition in (Al,Ga)As and correlation with the photoluminescence peak," *J. Appl. Phys.*, **57**, 512 (1985).

[8] H. J. Leamy, "Cathodoluminescence scanning electron microscopy of semiconductors," *J. Appl. Phys.*, **53**, R51 (1982).

[9] L. C. Kimerling, P. Petroff, and H. J. Leamy, "Injection-stimulated dislocation motion in semiconductors," *Appl. Phys. Letts.*, **28**, 297 (1976).

[10] D. Guidotti, E. Hasan, H. J. Hovel, and M. Albert, "Degradation of band-gap photoluminescence in GaAs,"*Appl. Phys. Lett.*, **50**, 912 (1987).

[11] A. K. Saxena, "Electron mobility in $Al_xGa_{1-x}As$ alloys," *Phys. Rev. B*, **24**, 3295 (1981).

[12] H. J. Lee, L. Y. Juravel, J. C. Woolley, and A. J. SpringThorpe, "Electron transport and band structure of $Al_xGa_{1-x}As$ alloys," *Phys. Rev. B*, **21**, 659 (1980).

[13] H. C. Casey, Jr. and M. B. Panish, *Heterostructure Lasers* (Academic Press, New York, 1978).

[14] S. Adachi, "GaAs, AlAs, and $Al_xGa_{1-x}As$: Material parameters for use in research and device applications," *J. Appl. Phys.*, **58**, R1 (1985).

Chapter 5

Effect of Al Mole Fraction on Carrier Diffusion Lengths and Lifetimes in $Al_xGa_{1-x}As$

5.1 Introduction

Measurement of certain basic material parameters such as carrier diffusion length, lifetime, and mobility is important for device modeling and material characterization. The $Al_xGa_{1-x}As$ system is an important material system for photonic applications such as lasers, light emitting diodes (LED), and photovoltaic devices, as well as electronic devices such as high electron mobility transistors, and resonant tunneling diodes. Although the electron mobility as a function of Al mole fraction has been studied systematically [1], reports of lifetimes or diffusion lengths in $Al_xGa_{1-x}As$ are scattered [2,3] and performed at lower excitation levels than those used in LEDs and lasers. In this chapter, we report on measurements of the ambipolar diffusion length and carrier lifetime in $Al_xGa_{1-x}As$ for several values of x in the interval $0 < x \leq 0.38$. Both the diffusion length and the lifetime show a dramatic increase for Al mole fraction near 0.4. Based on a consideration of the relative electron densities in the direct and indirect valleys, the increase in lifetime is attributed to population of the indirect valleys for $x \approx 0.4$.

5.2 Carrier Diffusion Lengths

The samples used in this experiment were grown by molecular beam epitaxy in a Riber 2300 R & D system. Layers with Al mole fractions of 0.09, 0.19, 0.25, 0.35, and 0.38 were grown as well as a GaAs layer and a 100Å GaAs quantum well. There was no intentional doping in any of the samples. The determination of the Al mole fraction was accomplished by room temperature photoluminescence (PL) measurements as described in Section 4.4. Determination of the ambipolar diffusion length was accomplished by a cathodoluminescence (CL) technique described in Chapter 4. Figure 5.1 shows the results of the diffusion length measurements. These data were taken at room temperature at carrier densities in the range of 10^{17} - 10^{18}cm^{-3}. For Al mole fraction less than 0.3, the diffusion length remains fairly constant, but for larger values of x, it shows an abrupt and large increase. The increase in the diffusion length implies an increase in either mobility or lifetime because $L_D = \sqrt{D\tau} = \sqrt{k_B T \mu\tau/q}$, where L_D, D, and μ are the ambipolar diffusion length, diffusivity, and mobility, and where τ, k_B, T, and q are the carrier lifetime, Boltzmann's constant, temperature,

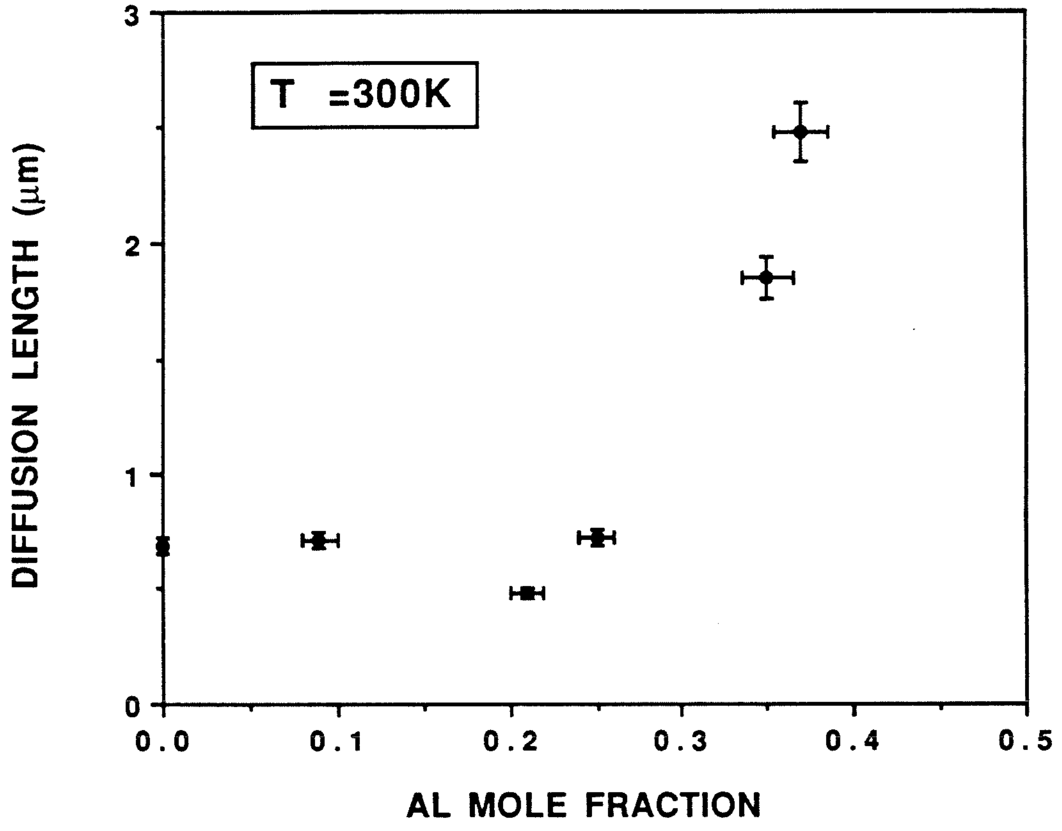

Figure 5.1: Ambipolar diffusion length at a carrier density of 10^{17}–10^{18}cm^{-3}. The samples with Al mole fraction greater than 0.3 have high values due to the increased lifetime. A 100Å GaAs quantum well showed the same value as the thicker GaAs ($x = 0.0$) layer.

and the electron charge, respectively. It is not unreasonable to expect the lifetime to increase as x approaches 0.4 because this is near the point at which AlGaAs becomes an indirect gap semiconductor and lifetimes in the indirect valleys can be quite long if the material is of good quality. Using the electron mobility data of Ref. [1], and a heavy hole mobility calculated from Ref. [6], our L_D measurements imply an order of magnitude increase in lifetime for the 0.35 and 0.38 Al mole fraction samples as compared to GaAs.

5.3 Carrier Lifetimes

To confirm our interpretation of the diffusion length data, carrier lifetimes were measured by examining the photoluminescence decay signal produced by short-pulse optical excitation of the sample. In this experiment, the sample was excited using frequency doubled pulses from a mode locked Neodymium YAG laser. The laser pulses typically had a 100ps width and a peak power of 1W. An electro-optic pulse extractor reduced the repetition rate from 100MHz to 10kHz. The luminescence was coupled into a monochromator, which acted as a bandpass filter, passing only the luminescence from the region of interest. The luminescence decay was measured with a photomultiplier tube and a boxcar integrator. The system response was measured to be 4ns.

The results of the lifetime measurement are summarized in Fig. 5.2. These data were taken at a carrier density of approximately $3\text{x}10^{18}\text{cm}^{-3}$. The samples with Al mole fraction less than 0.3 all showed a lifetime at the system limit of 4ns. Reports

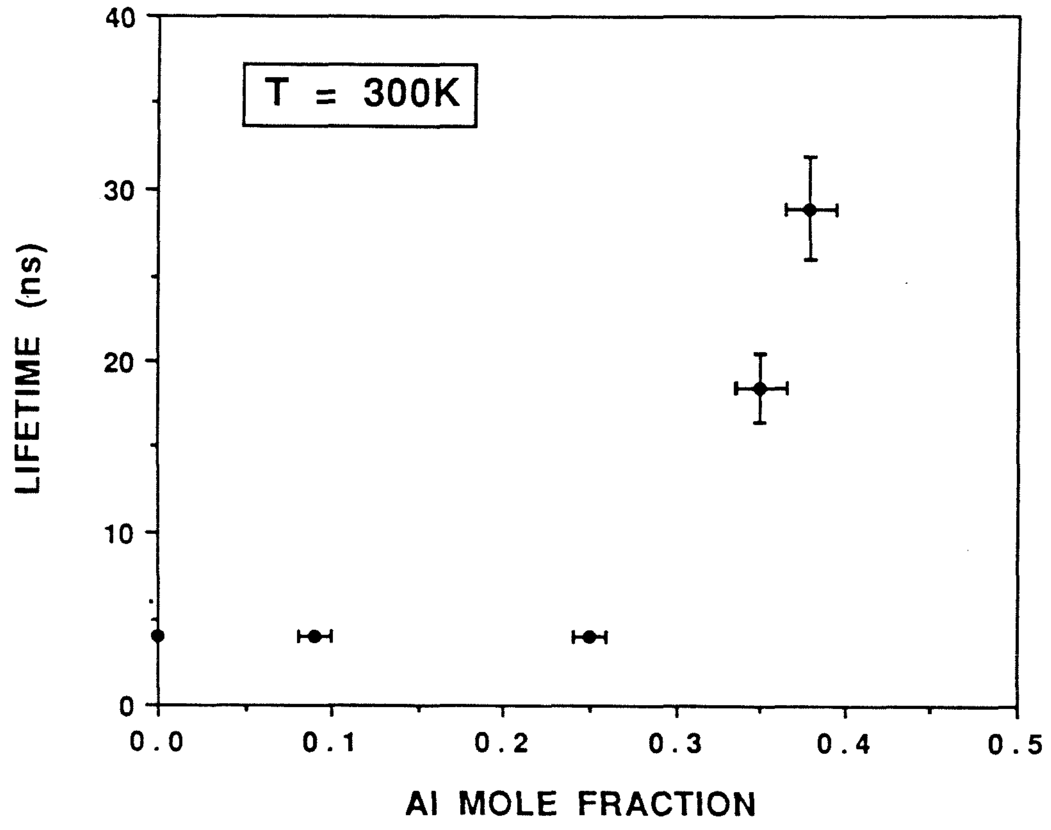

Figure 5.2: Carrier lifetimes at a carrier density of approximately 3 x 10^{18}cm^{-3}. The long lifetimes for the 0.35 and 0.38 mole fraction samples are attributed to population of the X and L valleys. The values for the samples with Al mole fraction less than 0.3 are upper limits because the system response was 4 ns.

on GaAs lifetimes for this carrier density are in the 2–4 ns range [4,7]. Lifetimes on the 0.35 and 0.38 mole fraction samples are an order of magnitude higher than this, in agreement with the predictions from the diffusion length measurements. These samples also showed a trend of increasing lifetime as the pumping power was increased, in apparent contradiction with expectations for a bimolecular recombination process. In the following section, we explain these effects by examining the relative populations of the direct and indirect valleys.

5.4 Lifetime Enhancement

As the Al mole fraction increases from zero to 0.35, the energy separation between the Γ, X, and L valleys decreases to less than 0.05eV [4,5]. This situation persists over the range $0.35 < x < 0.45$. In this region, all three valleys will be significantly populated under room temperature excitation. This is illustrated in Fig. 5.3, which shows the gap energies of the three conduction band valleys as a function of Al mole fraction as determined by Lee [5][1]. Because intervalley scattering and intraband relaxation processes all occur on a time scale that is much shorter than the carrier lifetime [8,9], the carriers in the conduction band may be assumed to be in thermal equilibrium. To understand the effects of intervalley scattering on carrier lifetimes, we start with the rate equations for the population of each valley,

$$\frac{dn_\Gamma}{dt} = -\frac{n_\Gamma}{\tau_\Gamma} - (n_\Gamma - n_X)\gamma_{\Gamma X} - (n_\Gamma - n_L)\gamma_{\Gamma L} \tag{5.1}$$

---

[1] There is some disagreement as to the relationship between bandgap energy and Al mole fraction [4,5], particularly in the range $0.35 < x < 0.45$. We have used the relationship of Ref. [5] because it is more recent.

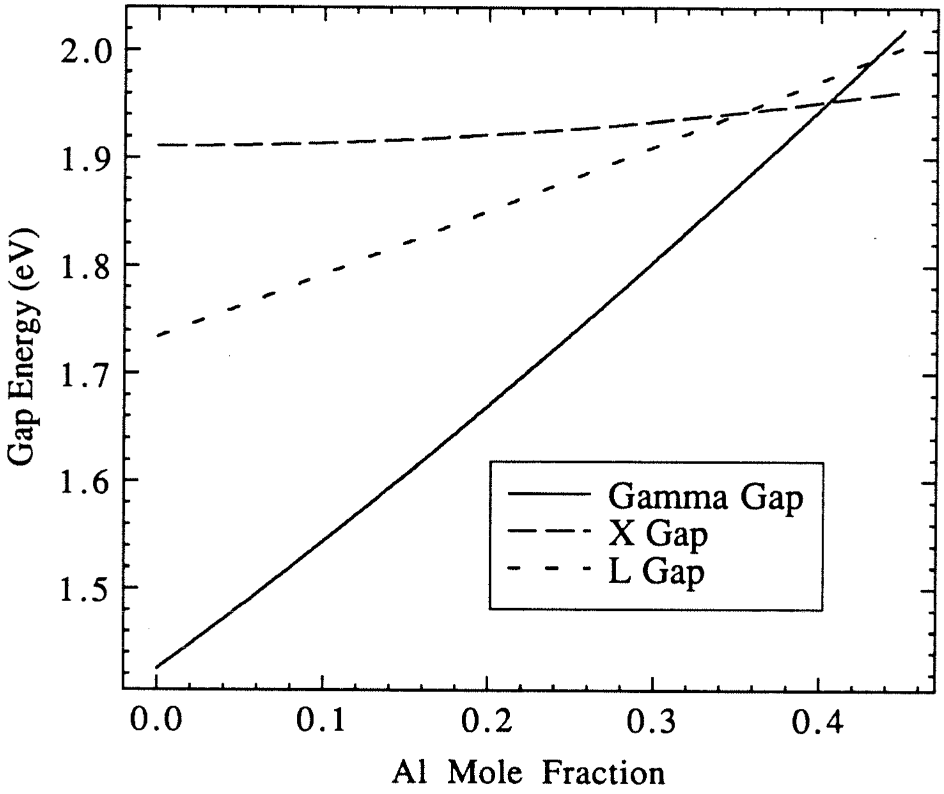

Figure 5.3: The gap energies for the Γ, X, and L valleys of $Al_xGa_{1-x}As$ as a function of Al mole fraction, x. These data are after Ref[5].

$$\frac{dn_X}{dt} = -\frac{n_X}{\tau_X} - (n_X - n_\Gamma)\gamma_{\Gamma X} - (n_X - n_L)\gamma_{XL} \tag{5.2}$$

$$\frac{dn_L}{dt} = -\frac{n_L}{\tau_L} - (n_L - n_\Gamma)\gamma_{\Gamma L} - (n_L - n_X)\gamma_{LX} \tag{5.3}$$

where the $n_{\Gamma,X,L}$ represent the populations of the three conduction band valleys, $\tau_{\Gamma,X,L}$ are the lifetimes of the carriers in the individual valleys due to recombination events in those valleys, and γ_{ij} are the scattering rates between valleys i and j, and it is assumed that $\Gamma_{ij} = \Gamma ji$. Adding these three yields the result

$$\frac{dn_\Gamma}{dt} + \frac{dn_X}{dt} + \frac{dn_L}{dt} = -\frac{n_\Gamma}{\tau_\Gamma} - \frac{n_X}{\tau_X} - \frac{n_L}{\tau_L} \tag{5.4}$$

in which all of the intervalley scattering terms have dropped out. The exclusion of these terms is no surprise because the left-hand side of Eq. 5.4 represents the rate of change of the total population of the conduction band, which is not affected by scattering events within the band. We now assume that the total population of the conduction band $n(t)$ can be characterized by a single lifetime τ. This requires the relative populations of the valleys to remain constant. Such a requirement is valid when the Fermi level is more than $2k_BT$ below the conduction band edge and is approximately true for the measurements here, as will be shown below (see Fig. 5.4). Under this assumption, the populations are given by

$$\begin{aligned} n_\Gamma(t) &= n_{\Gamma_0} e^{-t/\tau} \\ n_X(t) &= n_{X_0} e^{-t/\tau} \\ n_L(t) &= n_{L_0} e^{-t/\tau}. \end{aligned} \tag{5.5}$$

where n_{Γ_0,X_0,L_0} are constants. Putting Eq. 5.5 into Eq. 5.4 gives

$$\frac{1}{\tau} = \frac{n_\Gamma}{n}\frac{1}{\tau_\Gamma} + \frac{n_X}{n}\frac{1}{\tau_X} + \frac{n_L}{n}\frac{1}{\tau_L}, \tag{5.6}$$

which in the approximation

$$\frac{n_\Gamma}{\tau_\Gamma} \gg \frac{n_X}{\tau_X}, \frac{n_L}{\tau_L} \tag{5.7}$$

becomes

$$\tau = R\tau_\Gamma \qquad \text{where, } \mathrm{R} \equiv \frac{\mathrm{n}}{\mathrm{n}_\Gamma} \tag{5.8}$$

The parameter R can be viewed as a lifetime enhancement factor. On average, each electron will spend $1/R$ of its life in the Γ valley. Because recombination through the Γ valley dominates the population decay, the decay rate is reduced by the factor $1/R$. To calculate R we have calculated the populations of the three valleys of the conduction band using Fermi-Dirac statistics and the parabolic band approximation. The bandgaps for these valleys were taken from Ref. [5] and the density-of-states effective masses from Ref. [6]. In Fig. 5.4, $R(n)$ is plotted for Al mole fractions of 0.25, 0.35, and 0.38. At low carrier concentrations, the curves are flat because, in this region, the Fermi level is in the gap and the Fermi-Dirac distribution above the band edge is Boltzmann-like, leading to relative populations that are approximately independent of carrier density. For example, the relative population of the Γ and X valleys in this region is approximately given by $n_X/n_\Gamma = (m_X/m_\Gamma)^{3/2}e^{-\Delta E/k_BT}$, where m_X and m_Γ, are the density-of-states effective masses in the X and Γ valleys respectively and ΔE is the energy separation between the X and Γ band minima. As the Fermi level rises to within $2k_BT$ of the indirect valleys, R begins to increase sharply. This explains our observations of longer lifetimes for higher pump powers. Eventually, R begins to level off and approaches the value $(m_X + m_L + m_\Gamma)/m_\Gamma$ asymptotically. Although it is questionable whether these high carrier concentrations

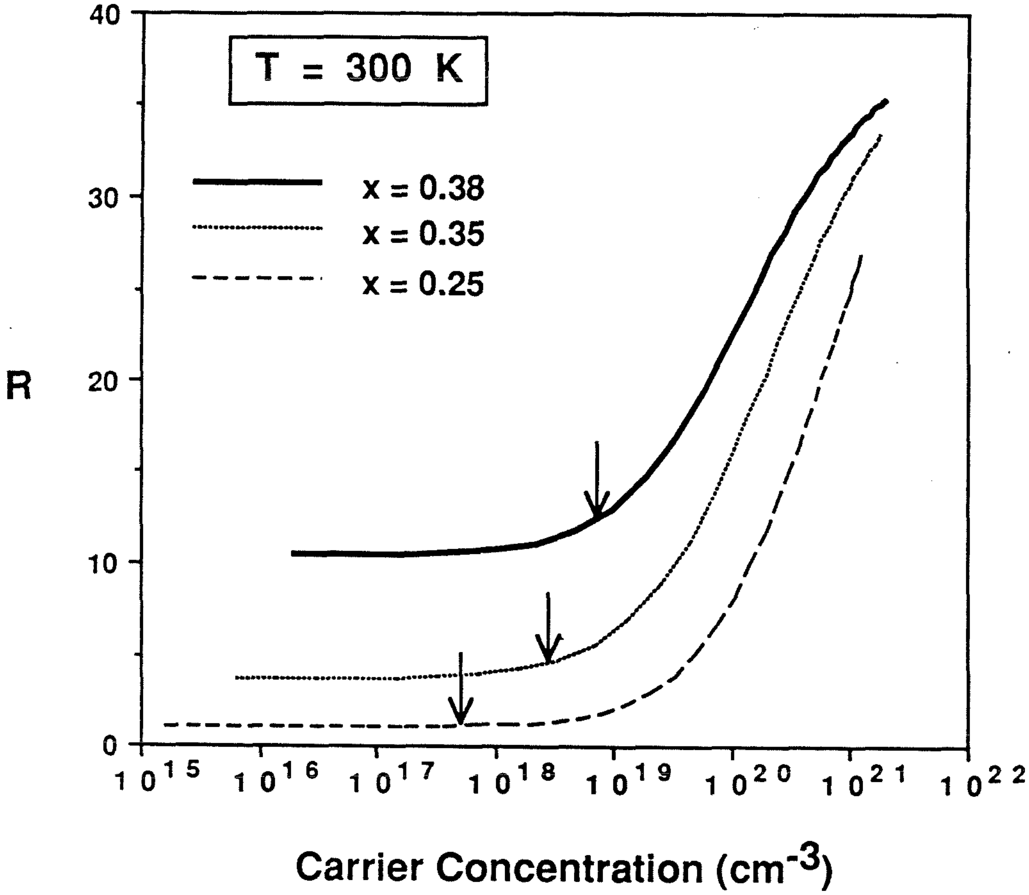

Figure 5.4: The ratio of the carrier concentration to the population of the Γ valley as a function of carrier concentration for three different Al mole fractions. The arrows show the concentration at which the quasi-Fermi level is at the bottom of the conduction band. The lower and upper endpoints of the curves correspond to quasi-Fermi levels 0.15eV below and 0.55eV above the conduction band edge.

could be achieved without other effects dominating, values of $R \geq 35$ should be attainable at lower carrier concentrations for slightly higher Al mole fractions. To compare these calculations with our data we assume a value for τ_Γ of 3ns. At a carrier concentration comparable to our experiments, this predicts lifetimes of 32, 12, and 3ns, in good agreement with our measured values.

5.5 Conclusions

In conclusion, we have presented measurements of ambipolar diffusion lengths and carrier lifetimes in $Al_xGa_{1-x}As$ for several Al mole fractions in the interval $0 < x < 0.38$. Samples having compositions near the direct gap–indirect gap transition show significantly increased lifetimes and diffusion lengths. We presented calculations indicating that, at these mole fractions, carriers are occupying states in the X and L valleys for a substantial fraction of their lifetime. These calculations indicate that the lifetime may be as long as 100ns with slightly higher mole fractions than investigated here. Measurements on the temperature dependence of the lifetime may prove useful in determining the composition at which $Al_xGa_{1-x}As$ becomes an indirect gap semiconductor.

Bibliography

[1] A. K. Saxena, "Electron mobility in $Al_xGa_{1-x}As$ alloys," *Phys. Rev. B*, **24**, 3295 (1981).

[2] R. K. Ahrenkiel, D. J. Dunlavy, R. Y. Loo, and G. S. Kamath, "Minority-carrier lifetime in n-$Al_{0.38}Ga_{0.62}As$," *J. Appl. Phys.*, **63**, 5174 (1988).

[3] G. W 't Hooft, C. van Opdorf, H. Veenvliet, and A. T. Vink, Minority carrier lifetime and luminescence in MOVPE-grown (Al,Ga)As epilayers and DH lasers," *J. Cryst. Growth*, **55**, 173 (1981).

[4] H. C. Casey, Jr. and M. B. Panish, *Heterostructure Lasers* (Academic Press, New York, 1978).

[5] H. J. Lee, L. Y. Juravel, J. C. Woolley, and A. J. SpringThorpe, "Electron transport and band structure of $Al_xGa_{1-x}As$ alloys," *Phys. Rev. B*, **21**, 659 (1980).

[6] S. Adachi, "GaAs, AlAs, and $Al_xGa_{1-x}As$: Material parameters for use in research and device applications," *J. Appl. Phys.*, **58**, R1 (1985).

[7] H. Namizaki, H. Kan, M. Ishii, and A. Ito, "Current dependence of spontaneous carrier lifetimes in GaAs-$Ga_{1-x}Al_xAs$ double -heterostructure lasers," *Appl. Phys. Letts.*, **24**, 486 (1974).

[8] C. L. Tang and D. J. Erskine, "Femtosecond Relaxation of Photoexcited Nonequilibrium Carriers in $Al_xGa_{1-x}As$," *Phys. Rev. Letts*, **51**, 840 (1983).

[9] J. Shah, A. Pinczuk, A. C. Gossard, and W. Wiegmann, "Energy-Loss Rates for Hot Electrons and Holes in GaAs Quantum Wells," *Phys. Rev. Letts.*, **54**, 2045 (1985).

Appendix A

Holographic Lithography Using the 2315Å Line of a Xe Ion Laser

The fabrication of structures showing quantum size effects such as quantum wires and quantum boxes requires lithographic techniques capable of generating patterns with a feature size of a few thousand angstroms or smaller. Lithographic patterns on this and smaller scales are also required for diffraction gratings in optoelectronic devices, such as distributed feedback lasers and distributed Bragg reflectors [1]. The generation of such fine patterns is generally accomplished either by electron beam lithography or by holographic lithography. In this section we report on the fabrication of 1180Å period gratings in polymethylmethacrylate (PMMA) using the 2315Å line of a Xe ion laser and a conventional holographic exposure setup. In such a setup, the period of the grating is given by the relationship

$$d = \frac{\lambda}{n\,(\sin\alpha - \sin\beta)}$$

where α and β are the angles of incidence of the two beams, n is the index of refraction, and λ is the wavelength of the light. The shortest period, $d = \frac{\lambda}{2n}$, is obtained for $\alpha = -\beta = \frac{\pi}{2}$. To reduce d, one can use a high index prism [2] or a shorter wavelength source. Unfortunately, coherent deep UV sources are not abundant. One approach is the generation of deep UV radiation as a harmonic of a powerful, lower frequency source [3].

The interference patterns were recorded on GaAs substrates, which were spin coated with a 1 percent solution of molecular weight 496K PMMA at 5000 RPM and prebaked at 170 C for 1 hr. Although usually used for electron beam lithography, PMMA has been shown to be sensitive to ultraviolet radiation with wavelengths of 2500Å and shorter [4]. In this region of the spectrum, the Novolac resists have a high absorption coefficient and a low bleachability making them unsuitable. After exposure, the samples were developed in methylisobutylketone (MIBK) for 60 seconds, rinsed sequentially in isopropanol and water, and blown dry with nitrogen. The samples were sputter coated with approximately 50Å of Au/Pd to prevent distortion of the images due to charging during observation by SEM.

Exposure of the PMMA was made with the 2315Å line of ionized xenon. This ultraviolet transition was first observed by Marling [5]; the energy level assignments are unknown, but the transition is usually attributed to doubly- or triply- ionized xenon, Xe III or Xe IV. A simple air-cooled, fused silica discharge tube 5mm inside diameter and 60cm long with ordinary fused silica Brewster's angle windows was used. A 10nF capacitor charged to 10 - 20kV was switched with a 5C22 thyratron to give

0.5μs, 800A discharge current pulses at about 40pps. A pair of mirrors peaked at 2310Å obtained from Acton Research Corp. provided the optical cavity: a 98 percent reflecting 2m spherical mirror and a 97 percent reflecting flat with 2 percent transmission. Lasing occurred for the second half of the current pulse, giving triangular pulses 0.25μs at the base. Average multimode output power was measured with an Epply thermopile at about 130μW, giving a peak power of about 25W with a duty cycle of 10^{-5}. An intracavity aperture was used to select TEM_{00} operation, with an estimated average intensity of 1.5mW/cm^2 at the center of the Gaussian. Because this particular laser transition exhibited optimum xenon pressures of 5 mtorr or less, gas cleanup by the discharge was relatively rapid; stable operation was obtained for about an hour at a time between gas refills. Because the power drifted somewhat during the exposure, the estimates of total energy deposition are approximate. If we assume that the ratio of the power in the two beams was two to one and we account for geometrical factors, the maximum intensity at the PMMA surface was 0.37 times that at the center of the Gaussian. This gives an intensity of 0.56mW/cm^2 in the center of the exposed regions. Exposure times of 2 to 10 minutes were used, with about 5 minutes giving the best results. A 5 minute exposure at 0.56mW/cm^2 corresponds to an energy deposition of 0.17J/cm^2. This estimate is considered to be good to within a factor of two.

Fig. A.1 shows a SEM micrograph of a 1180Å period grating in the exposed PMMA. This is close to the shortest period attainable with this laser without the use of a prism to shorten the wavelength. The flatness of the region between the stripes

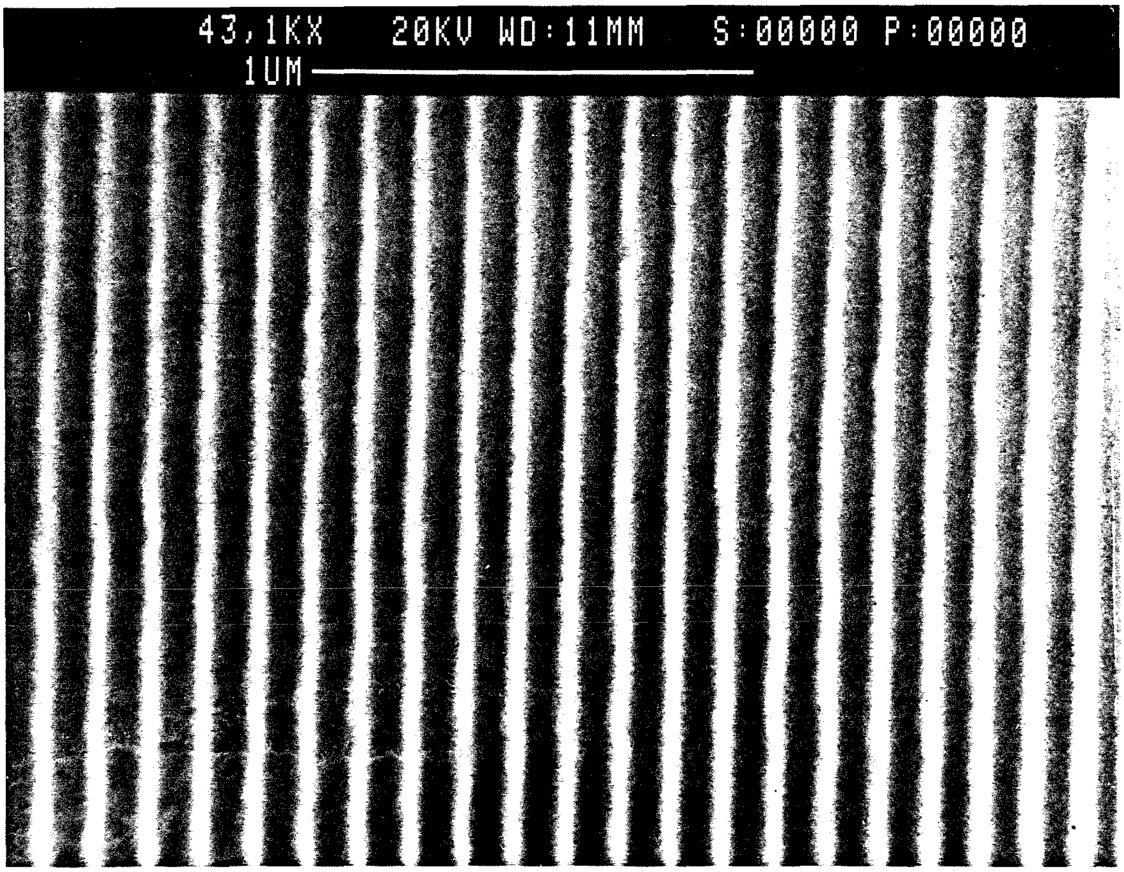

Figure A.1: SEM micrograph of 1180Å period grating in PMMA. Pattern was generated holographically with 2315Å emission from a Xe ion laser.

indicates that the exposure reaches the substrate. The grating pattern extends over an area of approximately 1mm^2, which corresponds to over 50 percent of the exposed area. Similar exposures were performed on a thin film of AZ1400 series resist, a Novolac resist, but the resulting resist profiles were poor and did not extend to the substrate.

In conclusion, a new source has been employed for deep UV holographic lithography and it has been shown to be capable of producing features as small as 600Å. A grating was produced with a period appropriate for use as a first order grating for a GaAs/AlGaAs distributed feedback laser. This technique may also be useful in the fabrication of quantum wires and quantum dots. The Xe ion laser, although not commercially available, can be assembled in the laboratory as an inexpensive UV source for lithographic purposes.

Bibliography

[1] A. Yariv, *Optical Electronics* (Holt, Rinehart, and Winston, New York, 1985).

[2] H. W. Yen, M. Nakamura, E. Garmire, S. Somekh, and A. Yariv, "Optically Pumped GaAs Waveguide Lasers With a Fundamental 0.11μm Corrugation Feedback," *Optics Comm.*, **9**, 35 (1973).

[3] G. C. Bjorklund, S. E. Harris, and J. F. Young, "Vacuum Ultraviolet Holography," *Appl. Phys. Lett.*, **5**, 451 (1974).

[4] B. J. Lin, "Deep UV Lithography," *J. Vac. Sci. Technol.*, **12**, 1317 (1975).

[5] J. B. Marling, "Ultraviolet Ion Laser Performance and Spectroscopy—Part I: New Strong Noble-Gas Transitions Below $2500\mathring{A}$," *IEEE J. Quantum Electronics* **11**, 822 (1975).